Flow and turbulence structure around an in-stream rectangular cylinder with scour hole

Gokhan Kirkil[1,2] and George Constantinescu[1]

Received 18 March 2010; revised 31 August 2010; accepted 24 September 2010; published 24 November 2010.

[1] Most of the erosion around obstacles present in alluvial streams takes place after the formation of a scour hole of sufficiently large dimensions to stabilize the large-scale oscillations of the horseshoe vortex (HV) system. The present paper uses eddy resolving techniques to reveal the unsteady dynamics of the coherent structures present in the flow field around an in-stream vertical cylinder (e.g., bridge pier) with a large scour hole at a channel Reynolds number defined with the channel depth and the bulk channel velocity of 2.4×10^5. The cylinder has a rectangular section and is placed perpendicular to the incoming flow. The geometry of the scour hole is obtained from an experiment conducted as part of the present work. The mechanisms driving the bed erosion during the advanced stages of the scour process around the vertical plate are discussed. Simulation results demonstrate the critical role played by these large-scale turbulent eddies and their interactions in driving the local scour. The paper analyzes the changes in the flow and turbulence structure with respect to the initial stages of the scour process (flat bed conditions) for a cylinder of identical shape and orientation. Results show the wake loses its undular shape due to suppression of the antisymmetrical shedding of the roller vortices. Also, the nature of the interactions between the necklace vortices of the HV system and the eddies present inside the detached shear layers (DSLs) changes as the scour process evolves. This means that information on the vortical structure of the flow at the initiation of the scour process, or during its initial stages, are insufficient to understand the local scour mechanisms. The paper also examines the effect of the shape of the obstruction on the dynamics of the vortical eddies and how it affects the bed erosion processes during the advanced stages of the local scour. In particular, the paper provides an explanation for the observed increase in the maximum scour depth for bed-mounted cylinders of rectangular section compared to cylinders of same width but of circular section. This increase is explained by the larger coherence of the HV system, the increased regularity of the interactions between the legs of the necklace vortices and the eddies shed in the DSLs, and the stronger coherence of the wake eddies, during both the initial and the later stages of the local scour process, for cases in which the obstruction has sharp edges that fix the separation point on the in-stream obstacle at all flow depths (e.g., rectangular cylinder).

Citation: Kirkil, G., and G. Constantinescu (2010), Flow and turbulence structure around an in-stream rectangular cylinder with scour hole, *Water Resour. Res.*, *46*, W11549, doi:10.1029/2010WR009336.

1. Introduction

[2] Natural river channels are subject to continuous change in geometry due to the interaction between the flow and erodible boundaries. The presence of large natural or man-made flow obstructions or large-scale bed roughness in alluvial channels induces local scour and greatly modifies the local structure of the flow and turbulence [see, e.g., *Roy et al.*, 2004; *Fael et al.*, 2006; *Hardy et al.*, 2007; *Lacey and Roy*, 2007]. Some of the most important applications are related to bridge pier and abutment scour due to the possible structural failure of bridges if local scour is too severe. A complex system of highly energetic turbulent structures is present around the in-stream obstruction and control the entrainment and transport of sediment from the scour hole. These highly energetic eddies (e.g., the necklace vortices that are part of the horseshoe vortex system) are much more coherent than the ones (e.g., eddies associated with the ejection and sweeps events) generally present in turbulent flows over a smooth or rough bed with fairly uniformly distributed roughness [see, e.g., *Ettema et al.*, 2006].

[3] The development of methods to predict the maximum scour depth around in-stream structures is one of the most intensive areas of research in river and coastal engineering (see, e.g., *Melville and Coleman* [2000] and *Sumer and Fredsoe* [2002] for a review of these methods). Despite the great deal of knowledge obtained from these studies, as discussed by *Yorozuya* [2005] and *Ettema et al.* [2006],

[1]Stanley Hydraulics Laboratory, Civil and Environmental Engineering Department, IIHR-Hydroscience and Engineering, University of Iowa, Iowa City, Iowa, USA.
[2]Now at Atmospheric, Earth and Energy Division, Lawrence Livermore National Laboratory, Livermore, California, USA.

0043-1397/10/2010WR009336

there are still important gaps remaining in understanding the main factors and processes influencing the mechanisms of local scour at bridge structures. In recent years there is a growing interest in developing scour prediction methods that incorporate the effect of the main eddies driving the scour into these prediction formulas [e.g., *Ettema et al.*, 2006]. To do that, one first needs to describe qualitatively and quantitatively the flow and turbulent structure at all the stages of the scour process [e.g., *Dey and Raikar*, 2007]. Then, based on this information, one can analyze the sediment entrainment mechanisms at play around obstructions of common shapes.

[4] For example, the experimental study conducted by *Dargahi* [1990] was one of the first to qualitatively document the changes in the scour mechanisms at a circular cylinder as the bed changed from flat to equilibrium scour. A main finding of his study was that no significant changes were observed in the structure of the horseshoe vortex (HV) system past the initial stages of the formation of the scour hole. Moreover, while during the initial stages scour was initiated at the sides of the cylinder by the strong acceleration of the flow as it passed the cylinder, in the later stages the HV system played the dominant role in the growth of the scour hole in front of the cylinder. Observations of the temporal evolution of the scour around cylinders showed that, once the scour hole has formed, the HV system becomes more stable, with most of the scouring taking place around the upstream base of the cylinder. However, the bed is scoured close to the cylinder at all polar angles. Thus, one needs to understand the dynamics of the coherent structures driving the scour around the obstacle for conditions that are far from those present at the initiation of scour. These findings motivate the present investigation in which the scour hole is representative of conditions present toward the end of the scour process.

[5] Experimental-based and/or numerical-based approaches that can resolve the unsteady dynamics of the large-scale turbulence can be used to obtain the detailed information needed to understand the mechanisms responsible for local scour around in-stream obstructions. Both approaches have advantages and disadvantages. So, ideally a joint approach would be the best way to proceed. The main advantage of using an experimental approach is that one can follow the time development of the local scour and visualize the direct effect of the eddies in the entrainment and transport of sediment particles from the mobile bed. In principle, this should also be possible using eddy resolving simulations with a movable bed. However, the uncertainties in modeling the transport of sediment particles in complex flows (e.g., within the scour hole), their interaction with the bed, and sediment entrainment in such numerical models are too large to have full confidence in these predictions. Of course, this approach should be pursued and the use of Reynolds Averaged Navier-Stokes (RANS) models coupled with sediment transport and a movable bed solver (see, e.g., *Roulund et al.* [2005] for a review of the relevant work in this area) replaced by Large Eddy Simulation (LES) or hybrid RANS-LES models, since the ultimate goal of such numerical simulations is the prediction of the flow and bed evolution from the start of the scour process until equilibrium scour conditions are reached. Careful validation of the models following this approach is needed.

[6] Obviously, experimental techniques do not face these limitations and are free of modeling errors. Such techniques were successfully applied to understand the mean flow and turbulent structure at cylindrical in-flow obstructions [see, e.g., *Yeh*, 1996; *Ahmed and Rajaratnam*, 1998; *Dey and Raikar*, 2007; *Raikar and Dey*, 2008; *Dey et al.*, 1995; *Graf and Istiarto*, 2002]. The study of *Dey and Raikar* [2007] was one of the few to provide detailed information on the changes of the mean flow and turbulence structure with the evolution of the scour hole (measurements with developing scour holes having depths of 0.25, 0.5, 0.75 and 1.0 times the depth at equilibrium scour were performed) at circular piers.

[7] Recently [e.g., *Unger and Hager*, 2006], more sophisticated techniques (e.g., Particle Image Velocimetry, PIV) that can capture both qualitatively and quantitatively the dynamics of these eddies were used to investigate the details of the flow physics. Though use of 2-D PIV techniques can greatly contribute to elucidating the turbulence structure around in stream structures placed on a mobile bed, they have some limitations. For example, such techniques do not allow bed shear stress in the instantaneous and mean flow fields to be accurately calculated, especially inside the scour hole where, due to the presence of strong adverse pressure gradients and flow separation, the logarithmic law is generally not valid. Also, 2-D PIV provides measurements in only a planar section at a time which, in a very complex turbulent flow, does not always allow one to easily understand the dynamics of the main eddies and their interaction. One should also mention that the use of recently developed 3-D PIV techniques [see, e.g., *Hinsch*, 2002] to study the flow around in-stream obstructions should remove, at least partially, this limitation. Unfortunately, no such studies are yet reported in the literature.

[8] Eddy resolving techniques conducted on sufficiently fine meshes can provide a detailed description of the dynamics of the coherent structures and accurately estimate quantities that are difficult to obtain from experiment [see, e.g., *Rodi*, 1997; *Krajnovic and Davidson*, 2002; *Keylock et al.*, 2005]. *Kirkil et al.* [2008] provide a detailed review of previous LES and hybrid RANS-LES investigations of flow past in-stream obstacles in a channel and discuss the main types of hybrid models for simulation of high Reynolds number turbulent flows. Few of these investigations [e.g., *Choi and Yang*, 2002; *Koken and Constantinescu*, 2008b; *Kirkil et al.*, 2009] were conducted with a deformed bed. Although in the case of calculations conducted with a fixed bed, the simulations cannot predict the evolution of the bathymetry around the obstructions, they can provide an accurate description of the flow and turbulent structure for a given bathymetry corresponding to a certain stage of the scour process. Fortunately, in most applications of interest in river and coastal engineering the time scales of the macroturbulence events and the time scales needed to calculate converged statistics are much smaller than the ones associated with significant changes in the bathymetry. For clear water scour one can also assume in a good approximation that the entrained sediment has a negligible effect on the dynamics of the coherent structures. Thus, provided that the bathymetry is available from experiment and the characteristics of the incoming turbulent flow are similar to those present in the experiment (see discussion of *Kirkil and Constantinescu* [2009]), eddy resolving techniques should be able to capture the dynamics of the energetic coherent structures in the flow and their effect on the mean flow, turbulence statistics, and bed shear stress distributions. Under some assumptions (e.g., the

flow within the bed is not significantly affecting sediment entrainment potential), this information (e.g., distributions of the shear stress and pressure rms fluctuations at the bed) can then be used to understand sediment entrainment processes. This is the approach adopted in the present study.

[9] This study considers the case of a cylindrical obstruction of a rectangular section mounted at the bottom of a straight channel with a fully developed incoming turbulent flow. The study compares present results with those previously obtained for circular cylinders. The channel Reynolds number defined with the channel depth, H, and the bulk channel velocity, U, is high enough ($Re_H = 2.4 \times 10^5$) to be representative of field conditions for small streams. The cylinder has a rectangular section with a relatively high aspect ratio (width to thickness ratio is approximately 14.5). The obstacle geometry is close to that of a wide bridge pier of intermediate width according to the classification of *Melville and Coleman* [2000]. Though several studies [e.g., *Laursen and Toch*, 1956; *Ettema et al.*, 1998] have investigated the variation of the scour depth with the angle of attack and the increase of the maximum scour depth compared to the case of a circular cylinder of same equivalent (projected) width, no clear explanation is still available for the mechanisms and processes that are responsible for the differences in the scour depths. Most scour prediction formulas rely on scour prediction at piers of circular section and use a shape coefficient to account for the increase of the maximum scour depth at piers of noncircular sections [see, e.g., *Melville and Coleman*, 2000].

[10] In the present study we consider the extreme case, where an obstacle is placed perpendicular to the flow. Since for this orientation the bluntness of the obstruction is the highest, the largest scour depth will occur. The bathymetry corresponds to conditions close to equilibrium scour. Understanding the flow and turbulence structure for cases in which a relatively large scour hole is present is essential to explain local scour processes, as most of the scour occurs after the scour hole is large enough to stabilize the large-scale oscillations of the horseshoe vortex (HV) system that drives the scour in front of the obstruction. Moreover, the development of a scour hole modifies the sediment entrainment mechanisms on the sides and behind the obstruction with respect to conditions present at the start of the scour. The mechanisms at the start of the scour process were investigated for the same obstruction of rectangular section in the companion paper by *Kirkil and Constantinescu* [2009]. Besides revealing interesting similarities in the structure of the HV system forming at the base of a rectangular cylinder and of a sidewall-mounted vertical wall obstruction (e.g., an abutment), a main finding of their study was that in the case of a rectangular cylinder with a high angle of attack the wake flow close to the bed remains supercritical. Consequently, the wake rollers are much more coherent and induce significantly larger bed shear stresses as they are advected downstream compared to the case of a circular cylinder. This provided an explanation for the much higher rate at which the scour hole grows behind a rectangular cylinder during the initial stages of the scour process. Though motivated primarily by bridge pier scour, as detailed by *Kirkil and Constantinescu* [2009], the relevance of the present study is wider (e.g., flow past in-stream natural or artificial islands of elongated shape present in shallow streams).

[11] Several main questions related to the physics of the scour process around large in-stream obstructions of cylindrical shape can be formulated. Among them are (1) which are the main eddies and flow features that drive the bed erosion process?; (2) are these eddies present and do they play an important role at all stages of the scour process?; (3) what are the reasons the scour is larger at obstacles with a rectangular section compared to obstacles with a circular section or with smoothed edges?

[12] Only partial answers are known to these questions. The present paper makes an attempt to give more complete answers to these questions based on results of eddy resolving simulations.

[13] We try to formulate answers by focusing on the processes that drive the formation of the large-scale energetic structures in the flow and by showing the direct link between the presence of a certain eddy and its effect on the bed. In this regard, sufficiently resolved eddy-resolving simulations have an important advantage over experimental investigations. Eddy resolving simulations provide the whole three-dimensional (3-D) instantaneous flow field and allow determining the distributions of the bed-friction velocity in the mean flow and of the pressure root-mean-square (rms) fluctuations at the bed. The distributions of the last two variables are critical in assessing regions where the bed will be eroded. Moreover, using the 3-D flow fields one can visualize the main eddies, characterize their shapes and their positions relative to the bed and, equally important, determine rather accurately the bed-friction velocity distribution at each instant in time. This allows establishing a direct link between the presence of a certain eddy in the flow and its capacity to erode the bed. In particular, one can explain how scour occurs in regions where the local time-averaged bed-friction velocity is below the threshold value for sediment entrainment. A relevant example is when an energetic eddy propagating in the bed vicinity induces values of the bed-friction velocity that are larger than the threshold value for sediment entrainment over a time that is larger than the one required for particle entrainment.

[14] The influence of the shape of the in-stream obstacle is discussed based on comparison of the present simulation results for a high aspect ratio rectangular cylinder with simulation results [*Kirkil et al.*, 2009] for a circular cylinder with a large scour hole. The diameter of the circular cylinder is equal to the width of the rectangular cylinder. In other words, the projected widths of the two cylinders in the direction perpendicular to the flow are equal. The flume and the channel Reynolds number were identical in the two simulations. Comparison of these two simulations should gives a better idea on the degree of similarity of the scour processes and the role played by the large-scale coherent structures at wide rectangular in-stream obstacles compared to obstacles of circular shape. This is important, as most of the scour formulas are calibrated based on experiments conducted for circular obstacles and consider the mechanisms driving the scour to be similar at obstacles of different shapes provided that the projected width is the same. The increased potential for scour induced by an obstacle with a higher degree of bluntness compared to that of a circular cylinder is accounted via a shape factor parameter in scour prediction methods.

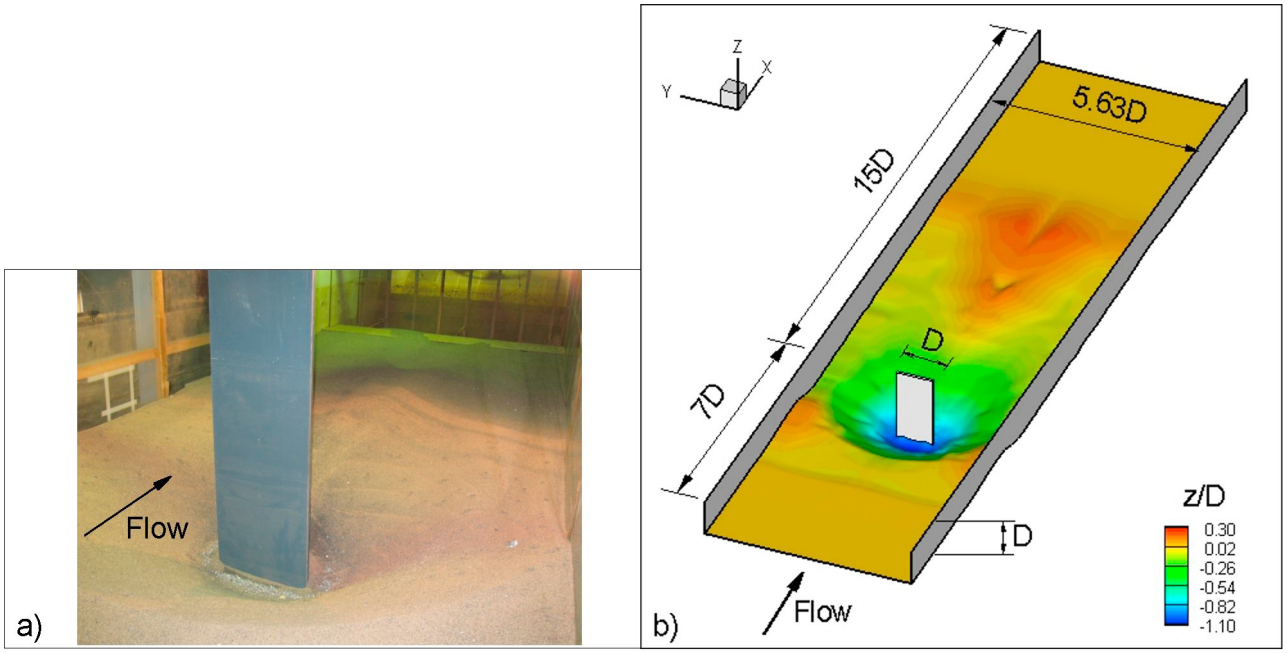

Figure 1. Bathymetry used in case RS. (a) Flume with scoured bed; (b) 3-D view of computational domain.

[15] In what follows, the numerical method, the experiment performed to obtain the bathymetry, and the set up of the simulation are discussed. This simulation of the flow past a rectangular cylinder with a large scour hole is referred to as case RS. Then, a full description of the flow and the unsteady dynamics of the large-scale coherent structures are provided for case RS, together with their effects on the distributions of the mean and instantaneous friction velocity and pressure rms fluctuations at the bed. Similarities and differences are discussed with respect to the flat bed case corresponding to conditions at the start of the scour process (case RF) and to the case of a circular cylinder with a large scour hole (case CS).

2. Flume Experiment

[16] Experiments were conducted in a flume 3 m wide and 2 m deep (see Figure 1a). Its test section is 20 m long. The width of the rectangular cylinder (D = 0.53 m), the flow depth (H = 0.53 m), and the mean incoming channel velocity (U = 0.45 m/s) were the same as the ones used in the flat bed experiment simulated in case RF. The thickness of the cylinder was 0.07D. The incoming flow was fully developed at the location of the cylinder. The main nondimensional flow parameters were $Re_D = Re_H = 240{,}000$ and $Fr_H = U/\sqrt{gH} \sim 0.2$, where g is the gravitational acceleration. Free surface deformations in the experiment were small. In the following discussion, the origin of the system of coordinates is located at the center of the rectangular cylinder at an elevation corresponding to that of the nondeformed bed.

[17] A uniform layer of sediment with a median diameter of d = 1.05 mm was placed on the bottom of the flume. The thickness of the sand layer was 1.0 m. The critical friction velocity was $u_{\tau c0}/U = 0.056$, where $u_{\tau c0}$ was estimated based on the Shields diagram. The experiment was conducted under clear water scour conditions and was run until the bed was close to equilibrium scour. This process took approximately five days.

[18] The equilibrium bathymetry is shown in Figure 1b. Due to the relatively large value of $u_\tau/u_{\tau c0}$ and small ratio between the width of the flume and that of the cylinder (close to 5.6), the scour hole extended laterally until close to the sidewalls. Two small deposition regions formed near the two sidewalls, slightly upstream of the section where the flow was obstructed by the presence of the rectangular cylinder. Similar to case CS, some contraction scour effects were present, but local scour remained the main mechanism responsible for the bed erosion.

[19] The maximum flow depth in the scour hole was 2.1D corresponding to a maximum scour depth of 1.1D. This value of the maximum scour depth relative to the flow depth away from the cylinder is within the range of values observed at bridge piers in the field. The scour depth nondimensionalized by the width of the cylinder, D, was close to 15% larger than the one (z/D = 0.97) observed in case CS (Figure 2b). The slope of the bed inside the deeper part of the scour hole in front of the cylinder was around 32°, which is 3° degrees smaller than the angle of repose of the sediment. Similar to case CS (Figure 2b), the scour hole was not as deep behind the cylinder, but extended to larger distances away from it.

[20] A deposition region in the form of a streamwise-oriented symmetric wedge (see Figure 1b) formed in the middle of the flume behind the cylinder starting at x/D = 3.5. Such deposition wedges are generally observed downstream of scour holes. They form due to the deceleration of the sediment particles entrained in the regions of high bed shear stress and pressure fluctuations around the cylinder. The deceleration occurs once the particles entrained by the various energetic eddies move sufficiently far downstream of the cylinder in a region where these eddies weaken and eventually dissipate.

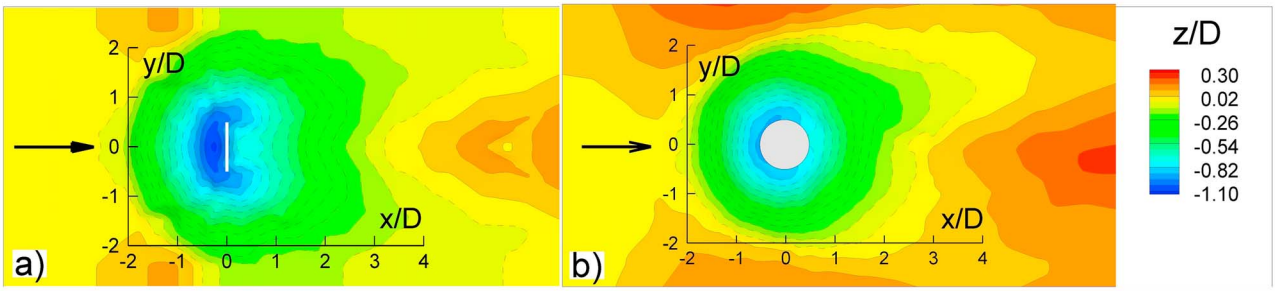

Figure 2. Comparison of nondimensional scour elevations (z/D < 0 indicates scour with respect to the initial flat bed level) in (a) case RS and (b) case CS.

[21] The bathymetry was measured in the horizontal directions on a grid with a spacing of 0.1 m. The data were then digitized for the purpose of generating the scoured bed surface used in the numerical simulation (Figures 1b and 2a).

3. Numerical Method and Simulation Set Up

[22] Due to the large value of the Reynolds number, Detached Eddy Simulation (DES) was used to perform the simulation. Hybrid RANS-LES techniques like DES [*Spalart*, 2000a]can resolve the dynamically most important eddies in the flow and allow studying the dynamics of the coherent structures at Reynolds numbers that are comparable to those encountered in the field. DES uses the same base turbulence model in the RANS and LES regions. No special treatment is required to match the solutions at the boundary between the LES and RANS regions. The model resolves the flow within the viscous sublayer, so the calculation of the bed shear stresses does not rely on the assumption of the presence of a logarithmic layer in the velocity profile.

[23] Detailed descriptions of the Spalart-Allmaras based DES model and the main features of the numerical method, which is second-order accurate in both space and time, are available in the companion paper by *Kirkil and Constantinescu* [2009] and are not repeated here. More details on the numerical method are given by *Constantinescu and Squires* [2004]. The code and the version of the DES model used to perform the simulation of case RS are the same as the ones used to perform the simulations of cases RF and CS.

[24] *Constantinescu and Squires* [2003, 2004], *Constantinescu et al.* [2003], and *Chang et al.* [2007] discuss results of grid sensitivity and validation studies for simulations of the flow past spheres and channel flow over a bottom cavity conducted using the same code. In particular, *Chang et al.* [2007] showed that the agreement between highly resolved LES and DES conducted on a much coarser mesh improved significantly when the inflow contained turbulent fluctuations obtained from a preliminary straight channel flow calculation. This is the approach adopted in the present study. It is consistent with the flow conditions present in the experiment and to the ones encountered in most applications of interest in river and coastal engineering, in which the incoming flow is strongly turbulent.

[25] One important issue is the capability of DES to capture the dynamics of the unsteady coherent structures in the flow past in-stream obstacles compared to LES. The related DES and LES studies of *Koken and Constantinescu* [2008a, 2009] for a vertical wall abutment placed in a straight channel (the shape of the obstruction was similar to the present rectangular cylinder, but the obstruction was mounted on one of the lateral walls of the channel) showed that the mean flow and turbulence statistics predicted by a DES simulation at a channel Reynolds number of 18,000 were very close to LES results at the same Reynolds number. The agreement between the two solutions was good despite the different numerics in the LES code, in which a fully nondissipative method was used to discretize governing equations, and the DES code, and the use of a RANS-based subgrid-scale model in DES instead of the dynamic Smagorinsky model in LES. A similar conclusion was reached by *Kirkil and Constantinescu* [2009], who performed LES and DES simulations for the case of a circular cylinder in a channel with a flat bed.

[26] The computational domain is shown in Figure 1b. The dimensions of the domain were chosen to correspond to the mobile bed experiment. As in the flat bed simulation (case RF), the domain width is 5.63-D. The computational domain extends 5D upstream of the rectangular cylinder and 15D downstream of it. The mesh contains 8.1 million cells (432 × 288 × 65 in the streamwise, spanwise and vertical direction, respectively). The first grid point off the solid surfaces is situated at approximately one wall unit ($\sim 5 \times 10^{-5}$ m). A hyperbolic tangent function was used to stretch the distribution of the mesh points away from all the solid surfaces. The cell spacing was 100–600 wall units inside the HV region. The grid spacing was around 20–100 wall units in the critical region situated around the two sides of the rectangular cylinder where the separated shear layers are forming. The average grid spacing was 500–2000 wall units in the near wake region, away from the rectangular cylinder.

[27] The procedure and data fields used to specify the velocity fields containing resolved turbulent fluctuations at the inflow section were identical to those used in case RF. The turbulent fluctuations (zero mean velocity) were obtained from a preliminary LES simulation of the flow in a straight channel conducted at a lower Reynolds number. The fluctuations were added to the RANS mean streamwise velocity profile obtained from a straight channel simulation at $Re_H = 2.4 \times 10^5$. The total velocity fields were then used to specify the inlet conditions in the simulation containing the cylinder. A convective boundary condition was used at the outflow.

[28] The free surface was modeled as a shear-free rigid lid. This is justified due to the low value of the Froude

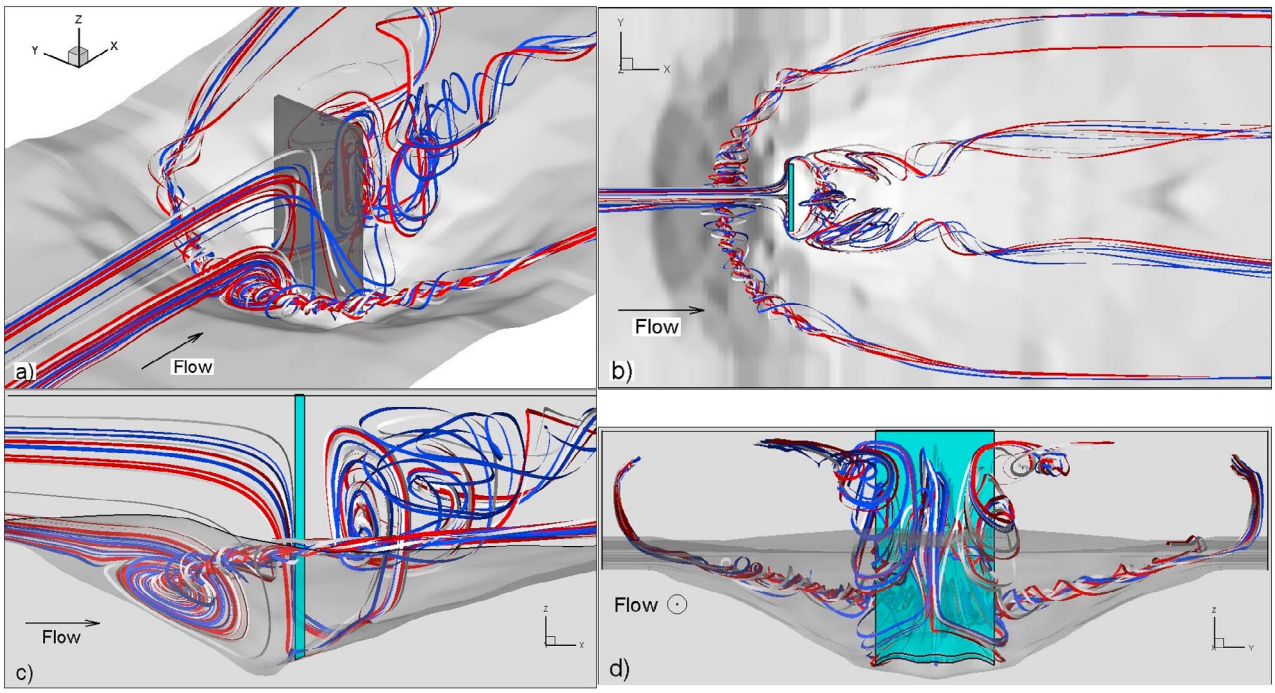

Figure 3. Visualization of the primary (HV1) necklace vortex and of the U-shaped vortex behind the cylinder in the mean flow using 3-D streamlines. (a) A 3-D view; (b) top view; (c) lateral view; (d) back view.

number, the absence of a bow vortex, and the small deformations of the free surface ($\Delta z/H < 0.055$) observed in the experiment conducted for the same flow conditions as the DES. A procedure similar to the one described by *Koken and Constantinescu* [2009] was used to confirm the validity of this modeling approach for the flow conditions considered in the present study for which the pressure distribution close to the free surface can be assumed to be close to hydrostatic. A main limitation of this approach is that it cannot be applied for supercritical flows, in fact for flows with Fr > 0.8, or in cases where a strong bow vortex forms beneath the free surface.

[29] The sidewalls, the channel bed, and the rectangular cylinder were treated as no-slip surfaces. To account for the small unresolved roughness in the bed-surface mesh, the modified eddy viscosity, $\tilde{\nu}$, at the wall was calculated such that the nondimensional bed roughness was close to 100 wall units. The value of $\tilde{\nu}$ on a rough wall is obtained from solving $\partial\tilde{\nu} / \partial n = \tilde{\nu} / n_1$, where n is the wall normal direction and n_1 is the distance to the wall for the first grid point off the wall surface [see *Spalart*, 2000b; *Zeng et al.*, 2008]. The time step in the simulation was 0.025 D/U.

4. Vortical Content of the Horseshoe Vortex System

[30] Figure 3a visualizes the main vortices present in the mean flow for case RS. The 3-D streamlines capture the presence of a large necklace vortex (HV1) inside the scour hole whose legs extend a large distance past the cylinder. The helicoidal trajectory of the streamlines inside the legs of HV1 (see Figures 3b–3c) indicates the coherence of the vortex remains high as it passes the cylinder. The discussion below focuses on the dynamics of HV1 in the instantaneous flow fields.

[31] Similar to the cases RF and CS, the dynamics of the HV system is controlled to a great extent by the large-scale bimodal oscillations of the core of HV1 and the associated temporal variations in the intensity of the jet-like flow beneath HV1. The jet-like flow forms due to advection of eddies first with the downflow, toward the toe of the cylinder, and then away from the cylinder's face and parallel to the deformed bed. The bimodal oscillations induce significant changes in the intensity of the jet-like flow and in the size and shape of the core of HV1. The core oscillates between two states called the zero-flow mode and the back-flow mode. The transition to the zero-flow mode is associated with the injection into the core of HV1 of a patch of low-momentum and high-vorticity fluid ejected from the separating incoming boundary layer. The transition to the back-flow mode is generally triggered by a patch of high-momentum and low-vorticity fluid (e.g., from the upper layer of the channel) that reaches the upstream face of the cylinder and is then transported with the downflow toward the channel bottom where it merges with the core of HV1.

[32] Consistent with previous experimental [e.g., *Devenport and Simpson*, 1990] and numerical investigations of flows past surface-mounted bluff bodies, in the zero-flow mode the core of HV1 is more circular, the jet-like flow beneath HV1 is weak, and a strong tongue of vorticity of opposite sign to that inside HV1 is ejected away from the bed. In the back-flow mode the core of HV1 is more elliptical, the jet-like flow is strong, and no tongue of vorticity of opposite sign to that inside HV1 is ejected away from the bed, which allows eddies from the incoming separated boundary layer to feed vorticity inside the upstream part of HV1.

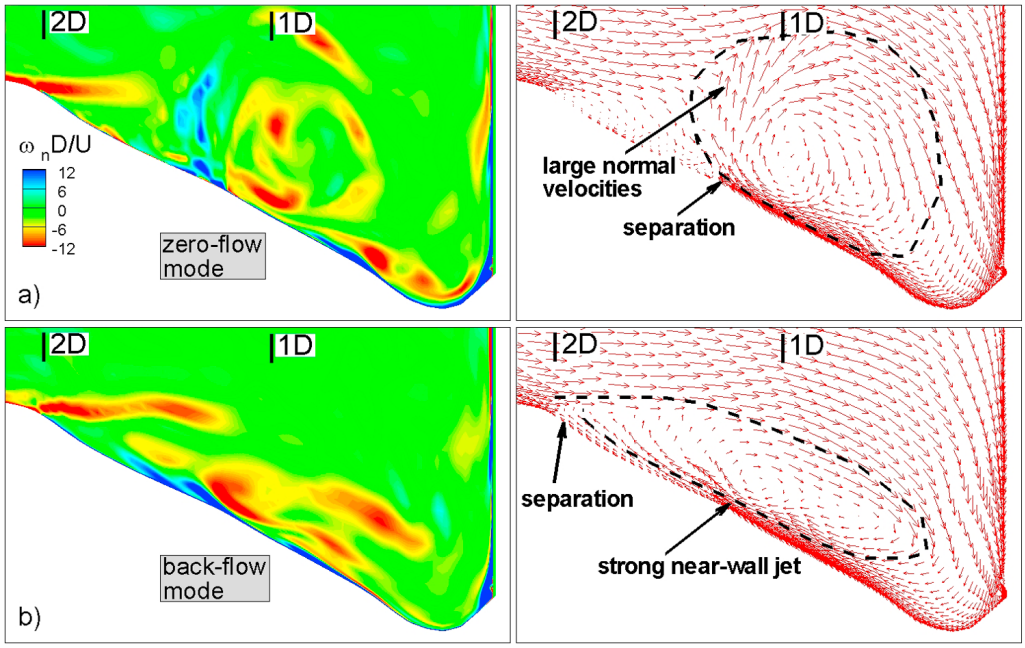

Figure 4. Visualization of the structure of the flow in (a) the zero-flow mode and (b) the back-flow mode using out-of-plane vorticity contours and instantaneous velocity vectors in the symmetry (y/D = 0.0) plane.

[33] The out-of-plane vorticity contours and velocity vector plots in Figure 4 visualize the structure of the flow in the symmetry (y/D = 0.0) plane when the HV system is in the zero-flow mode and in the back-flow mode, respectively. Consistent with cases CS and RF, the switching between the two modes does not take place at a well-defined frequency (the oscillations are aperiodic) and the velocity histograms in the region in which the core of HV1 oscillate are bimodal, in the sense that the probability density function of the velocity at stations situated within the core of HV1 has a two-peak shape. Outside of this region, the velocity histograms recover their usual one-peak shape. However, the flow structure inside the HV region as HV1 undergoes the bimodal oscillations has some particularities in case RS, as discussed below.

[34] Analysis of the out-of-plane vorticity contours in Figure 5 gives more detail on the way HV1 switches between the two modes in the symmetry plane. The shape of the core is elliptical and the elongated region of high vorticity inside the core of HV1 is parallel to the deformed bed. HV1 is in the back-flow mode. The intensity of the jet-like flow started to decay and a weak tongue of negative vorticity oriented away from the bed is already present (see arrow in Figure 5a). This tongue of vorticity does not allow the secondary eddies shed from the incoming separated boundary layer to merge with the eddies that are part of the core of HV1. The incoming separating boundary layer is one of the main sources of growth for HV1, as it contains vorticity of the same sign (positive) to the one inside the core of HV1. In Figure 5b, the strength (circulation) of the tongue of negative vorticity has grown. As the eddies containing positive vorticity from the incoming separated boundary layer approach the patch of negative vorticity, they are diverted toward the bed. This shows the transfer of vorticity from the incoming separated boundary layer toward HV1 is not continuous. In Figure 5c the tongue of negative vorticity is oriented away from the bed, but is still attached to the bed. It is surrounded by eddies containing positive vorticity from the core of HV1 on one side and from the incoming separated boundary layer on the other side. As the jet-like flow beneath HV1 is weak, the eddies convected with the jet-like flow accumulate inside the core of HV1 and increase its size. At this point, the transition to the zero-flow mode is basically complete (e.g., compare vorticity distributions in Figures 5c and 4a). The transition to the back-flow mode has started in Figure 5d and will end when a new tongue of negative vorticity forms and the eddies from the incoming separated boundary layer will not be able to feed directly positive vorticity inside the core of HV1.

[35] This mechanism of transition presents some differences with the classical one proposed by *Devenport and Simpson* [1990] for bluff bodies mounted on flat surfaces. The main difference is the important role played by the eddies shed from the incoming separated boundary layer and the way the eddies interact with the tongue of negative vorticity. The different dynamics of these eddies is obviously a consequence of the presence of a highly scoured bed in between the line where the incoming boundary layer separates and the upstream face of the cylinder. Additionally, the transition to the back-flow mode can also be triggered by the advection of high-momentum and high-vorticity eddies, first with the downflow toward the toe of the cylinder and then away from the cylinder, as part of the jet-like flow. As the downflow is stronger for cylinders with a higher degree of bluntness, in average, the momentum of the eddies injected into the main necklace vortices is also larger. This generally results in the formation of a more coherent main necklace vortex, a larger amplification of the turbulence in the region where bimodal oscillations are present (see discussion of Figure 9), a larger displacement of HV1 toward the mouth of the scour hole and/or the lifting of HV1 away from the bed. These phenomena explain why the bimodal oscillations are stronger

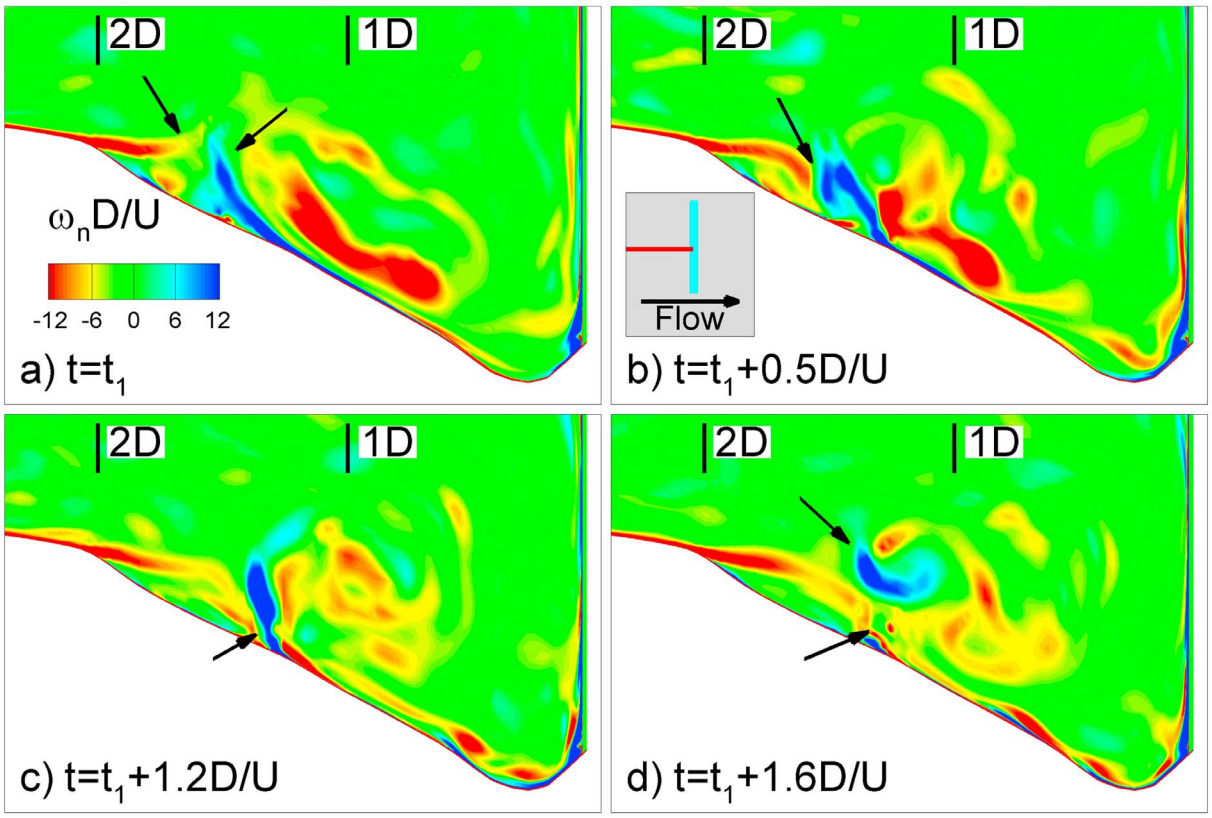

Figure 5. Visualization of the temporal evolution of the instantaneous structure of the HV system in the symmetry (y/D = 0.0) plane using out-of-plane vorticity contours. (a) Here $t = t_1 + 0D/U$; (b) $t = t_1 + 0.5D/U$; (c) $t = t_1 + 1.2D/U$; (d) $t = t_1 + 1.6D/U$.

for obstacles with a larger degree of bluntness. The increased erosion potential of HV1 eventually results into the formation of a larger and deeper scour hole at equilibrium conditions for obstacles with a larger degree of bluntness (e.g., by about 15% for the maximum scour depth for case RS compared to case CS).

[36] The horizontal vorticity contours in the instantaneous flow are shown in Figure 6 on a deformed surface situated everywhere at 0.07D from the channel bed. Besides the expected regions of high vorticity situated inside the upstream part of the scour hole that correspond to the necklace vortices, several elongated streaks of high vorticity are present inside the scoured hole, both on the sides and downstream of the cylinder. At most time instances these streaks are oriented parallel to the lines of constant bed elevation (dashed lines in Figure 6) and move against the local slope of the bed. One of the mechanisms responsible for the formation of these streaks is the curving of one of the legs of the necklace vortex toward the back of the cylinder (e.g., streak S1 on the right side of the cylinder) followed by the detachment of the downstream part of the leg and the advection of this streak of vorticity away from the cylinder (e.g., streak S2). The time scales associated with the formation of these streaks, the circulation within the core of the streaks, and their life time are highly variable. This is due to the large-scale oscillations of HV1, the temporal variations in the coherence of HV1 as it wraps around the base of the cylinder, and the random nature of the interactions between the legs of the necklace vortices and the surrounding eddies in the turbulent flow. The distance over which these streaks of vorticity travel before dissipating is also highly variable. The presence of these streaks inside the scour hole was also observed in case CS. Their dynamics was similar, though their coherence was, on average, weaker. This suggests that their dynamics are independent of the shape of the obstacle, past the initial stages of the scour process.

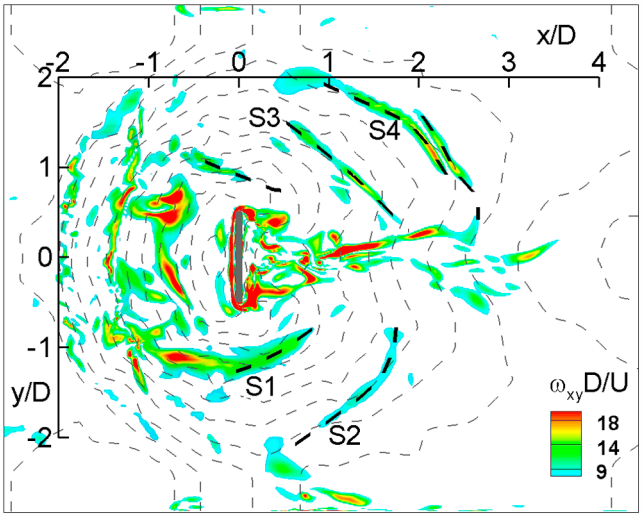

Figure 6. Horizontal vorticity contours in a deformed surface situated at $\Delta z_d = 0.07D$ from the deformed bed. The thick dashed lines highlight the near-bed vorticity streaks. The bathymetry isocontours are shown with thin dashed lines.

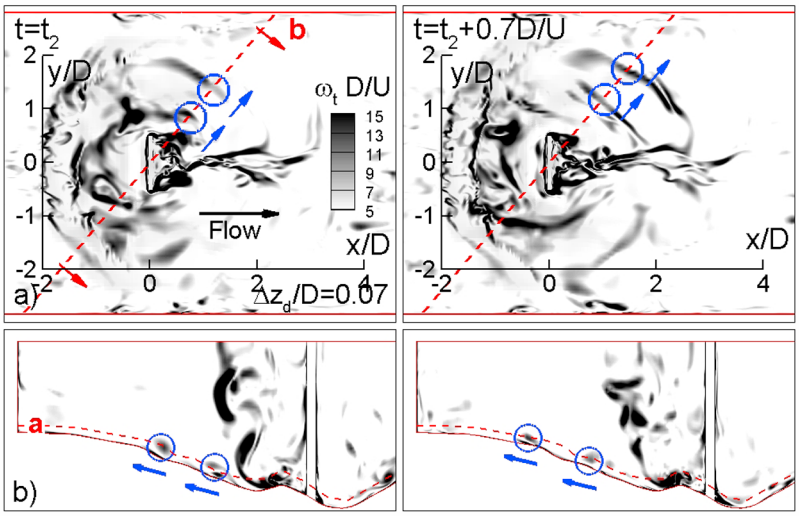

Figure 7. Visualization of the dynamics of the near-bed vorticity streaks in the instantaneous flow fields using vorticity magnitude ($\omega_t D/U$) contours. The left and right frames show the advection of the streaks away from the cylinder. (a) Deformed surface situated at $\Delta z_d = 0.07D$ from the bed; (b) vertical plane (see dashed line in Figure 7a) cutting the axes of two of the streaks (the circles indicates their position, the arrows indicate the direction of their movement) at an angle close to 90°.

[37] From time to time, an array of vortical streaks forms on one side of the cylinder. Such an event is visualized in Figure 7 that shows the advection of two streaks on the left side of the cylinder. As they are convected away from the cylinder, the streaks remain fairly parallel. The movement of the streaks against the local slope of the bottom increases the efficiency of the streaks in terms of their capability to entrain sediment particles from the deeper parts of the scour hole and to carry them toward the shallower regions. As it is fairly common for these streaks to extend until close to the symmetry plane behind the cylinder, the streaks play an important role in the growth of the scour hole not only laterally but also downstream of the cylinder.

[38] One of the mechanisms that is responsible for the detachment of streaks of vorticity from the legs of the necklace vortices is the advection of some of the eddies from the highly vortical region in between the two detached shear layers (DSLs) toward the bed. In some cases, the interaction of these eddies with the bed results in the formation of such streaks. Most of these eddies approaching the bed close to one of the DSLs are convected toward the symmetry plane. However, at times such eddies can be convected outward, away from the DSLs. The eddies present inside the recirculation region forming between the two DSLs move predominantly toward the free surface close to the symmetry plane, and toward the bed close to the sides of the recirculation region. This movement is consistent with the presence of the two strong streamwise oriented eddies behind the cylinder (Figure 3d). One common behavior of the streaks is that they do not switch from one side of the cylinder to the other as they travel downstream.

5. Mean Flow and Turbulence Statistics in the Horseshoe Vortex System Region

[39] Figure 8 visualizes the position of HV1 relative to the cylinder in the mean flow using the Q criterion [*Dubief and Delcayre*, 2000]. The invariant quantity Q is defined as $Q = -0.5\ \partial u_i/\partial x_j \cdot \partial u_j/\partial x_i D^2/U^2$ and identifies vortical structures within a velocity flow field. A secondary, much weaker, necklace vortex HV2 is present close to the mouth of the scour hole, at spanwise locations situated close to the symmetry plane. This vortex has the same sense of rotation as HV1. In the instantaneous flow, small secondary necklace vortices are detaching from the separating incoming boundary layer close to the mouth of the scour hole and are merging in an irregular way with HV1. The distributions of the turbulent kinetic energy (tke) and pressure root-mean-square (rms) fluctuations, p'^2, are shown in several vertical sections in Figure 9. The sections are perpendicular to the axis of HV1. Figure 9a corresponds to the symmetry plane, Figure 9c cuts through the lateral extremity of the cylinder and Figures 9d and 9e cut through the DSL. Both variables were nondimensionalized using a velocity scale defined as $u_s = \sqrt{(\rho_s/\rho - 1)gd}$, where ρ and ρ_s are the densities of the water and sediment, respectively. For the present simulation, $u_s = 0.29U$.

[40] The turbulence intensity inside the region where the core of HV1 undergoes bimodal oscillations is comparable in Figures 9a–9c. This is different from the variation

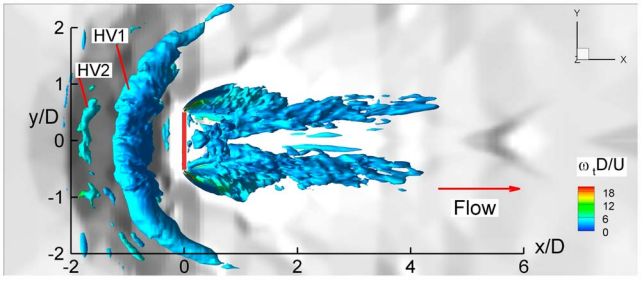

Figure 8. Visualization of the main (HV1) and secondary (HV2) necklace vortices and of the vortical content of the near wake in the mean flow using a Q isosurface ($Q = -0.5\ \partial u_i/\partial x_j \cdot \partial u_j/\partial x_i\ D^2/U^2$). The view is from above.

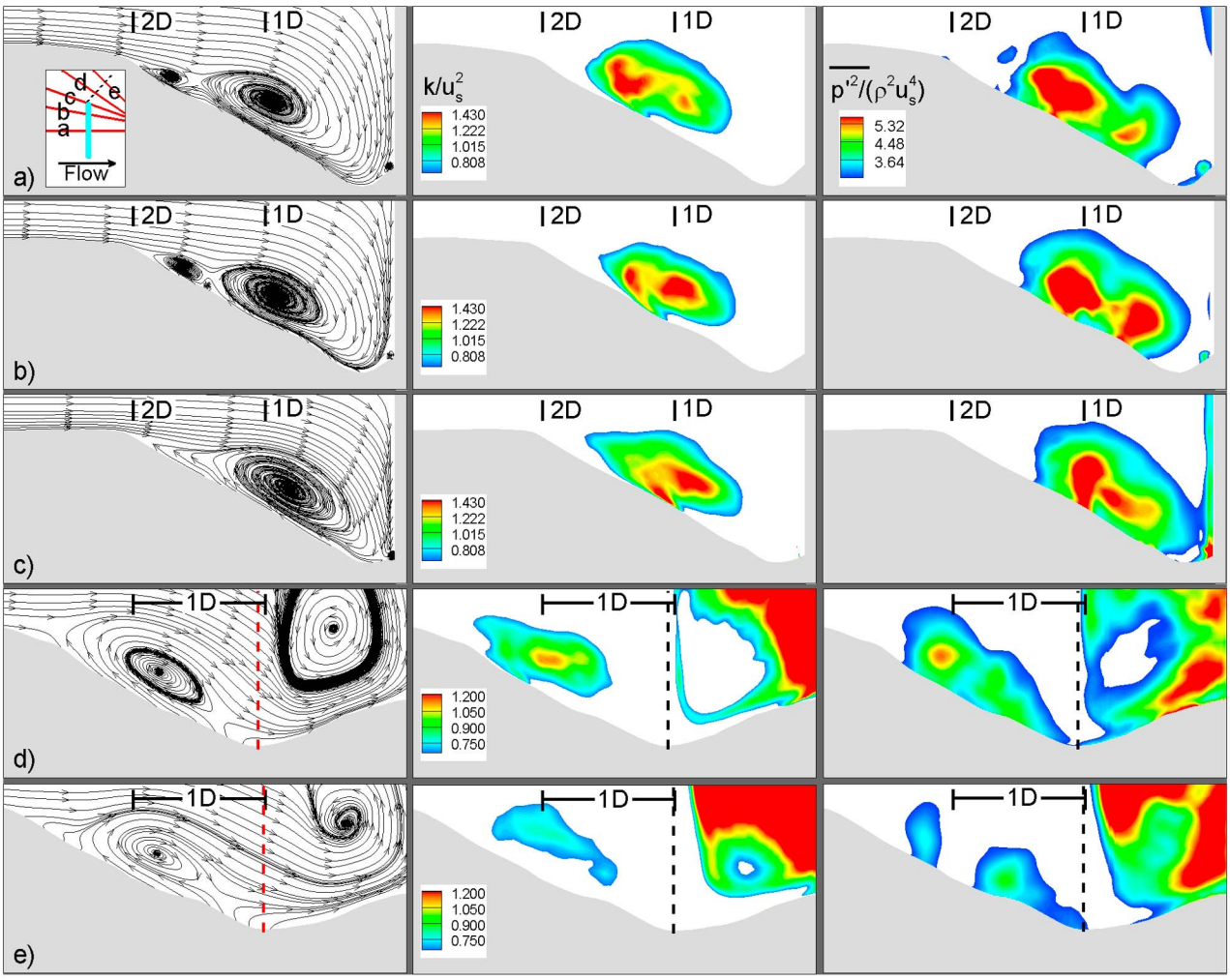

Figure 9. Mean flow 2-D streamline patterns and resolved tke and pressure rms fluctuations. The positions of Figures 9a–9e relative to the rectangular cylinder are shown in the inset in Figure 9a. The dashed vertical line in Figures 9d and 9e corresponds to the extremity of the DSL close to the free surface. The velocity scale used to nondimensionalize the turbulence quantities is $u_s = \sqrt{(\rho_s/\rho - 1)gd} = 0.29U$.

observed in case CS, where the turbulence intensity decayed with the magnitude of the polar angle starting at the symmetry plane. Then, a clear decay of the turbulence intensity is observed in Figures 9d and 9e, as HV1 is swept past the rectangular cylinder.

[41] The nondimensional tke values inside the core of HV1 in the region situated in front of the cylinder are more than two times larger than the ones observed in case CS [see *Kirkil et al.*, 2009, Figure 9]. The tke distributions in Figures 9a–9c are qualitatively similar. The elliptical region of high tke present away from the bed is induced by the switching of the core of HV1 between the zero- and the back-flow modes. A second patch of high tke is present close to the bed, around the place where a tongue of vorticity of opposite sign to than inside HV1 is ejected from the bed, as HV1 starts switching from the zero-flow mode to the back-flow mode. This distribution is qualitatively similar to the one observed for $|\varphi| < 30°$ [*Kirkil et al.*, 2009, Figure 9] in case CS. The strong tke amplification in the region where a tongue of vorticity is ejected away from the bed was also observed in the tke distribution measured in the symmetry plane of a wing-shaped body at a comparable Reynolds number by *Devenport and Simpson* [1990]. As HV1 is swept past the sides of the cylinder, the region of high tke amplification moves away from the bed (Figure 9e). The streamwise decay of the tke inside the legs of HV1 is relatively sharp and is related to the decay in the amplitude of the bimodal oscillations. This behavior is similar to the one observed in case CS.

[42] The distributions of $\overline{p'^2}$ in Figure 9 show that while the pressure rms fluctuations are amplified in the region in which the core of HV1 oscillates between the two modes, relatively large levels are also present inside the jet-like flow. In fact, as one moves away from the symmetry plane, the size of the region associated with the jet-like flow, where the $\overline{p'^2}$ levels are significantly above the background levels, becomes eventually larger than the one associated with the lateral oscillations of the core of HV1 (e.g., this is the case at Figure 9c). Also important for sediment entrainment in this region of the scour hole is the fact that the regions of high $\overline{p'^2}$ penetrate up to the bed surface, especially in the region associated with the jet-like flow. Meanwhile, the levels of

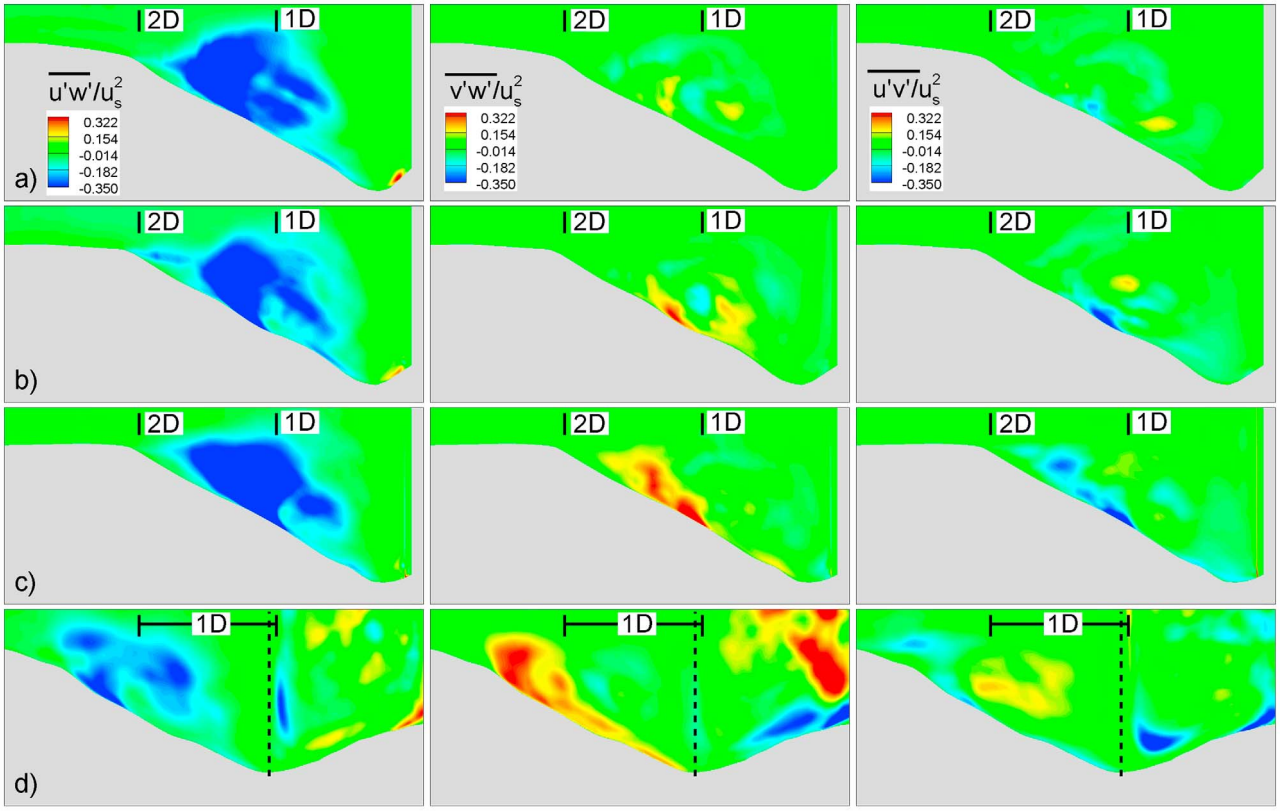

Figure 10. Reynolds shear stresses (left) $\overline{u'w'}$, (middle) $\overline{u'v'}$, and (right) $\overline{v'w'}$. The positions of Figures 10a–10d relative to the rectangular cylinder are shown in the inset in Figure 9a. The dashed vertical line in Figure 10d corresponds to the extremity of the DSL close to the free surface. The velocity scale used to nondimensionalize the Reynolds stresses is $u_s = \sqrt{(\rho_s/\rho - 1)gd} = 0.29U$.

$\overline{p'^2}$ remain relatively low in the downflow parallel to the upstream face of the cylinder.

[43] This is in contrast to the distributions of $\overline{p'^2}$ in case CS where, in sections with a low magnitude of the polar angle ($|\varphi| < 30°$), the pressure rms fluctuations were the largest in the region where the eddies advected with the downflow reached the bed. The main difference between the two cases is that the levels of $\overline{p'^2}$ inside the region associated with the bimodal oscillations of HV1 are couple of times lower in case CS compared to those predicted in case RS. Such an amplification was however observed in sections of low magnitude of the polar angle in a simulation of the flow past a circular cylinder conducted at a much smaller Reynolds number (Re_D = 16,000) by *Kirkil et al.* [2008]. It is only at sections cutting through the upstream part of the DSL (e.g., Figure 9d) and through the legs of HV1 (e.g., Figure 9e) that the distributions of $\overline{p'^2}$ in case RS become qualitatively similar to the ones in case CS. In these sections the regions of high tke do not correlate with those of high $\overline{p'^2}$, the latter being situated much closer to the bed and the DSL. This shows the high complexity of the turbulence structure in these flows and questions the utility of simplified conceptual models that assume that the pressure fluctuations are high in regions where the tke or the velocity fluctuations in the direction normal to the bed are high.

[44] Figure 10 presents the distributions of the nondimensional Reynolds shear stresses. As expected, the dominant shear stress term in the symmetry plane is $\overline{u'w'}$, with the other two terms provide negligible contributions (Figure 10a). The region of high negative values of $\overline{u'w'}$ correlates well with the region of high tke values in Figure 9a. The only difference is that the magnitude of $\overline{u'w'}$ remains high inside the upstream part of the jet-like flow. As one moves away from the symmetry plane (Figures 10b and 10c), the region of high negative values of $\overline{u'w'}$ correlates even better with the region of high tke values (Figures 9b and 9c). Meanwhile, the distributions of the other two shear stresses show relatively large values within part of the scour hole. This is primarily due to the fact that the core of the main necklace vortex is not anymore parallel to the spanwise (y) direction. The shear stress component associated with the correlation between the vertical velocity fluctuations and the velocity fluctuations in the direction perpendicular to the axis of the main necklace vortex is the dominant shear stress in sections situated away from the symmetry plane. Interestingly, the regions of high absolute values of $\overline{v'w'}$ and $\overline{u'v'}$ are confined to the near bed region and are induced by the changes in the penetration distance of the jet-like flow beneath HV1 during the bimodal oscillations. The magnitude of $\overline{u'w'}$ decays fast in sections cutting the shear layers (Figure 10d), while that of $\overline{v'w'}$ increases both beneath and upstream of HV1. This is because past Figure 10c the oscillations of HV1 have a strong lateral component. The

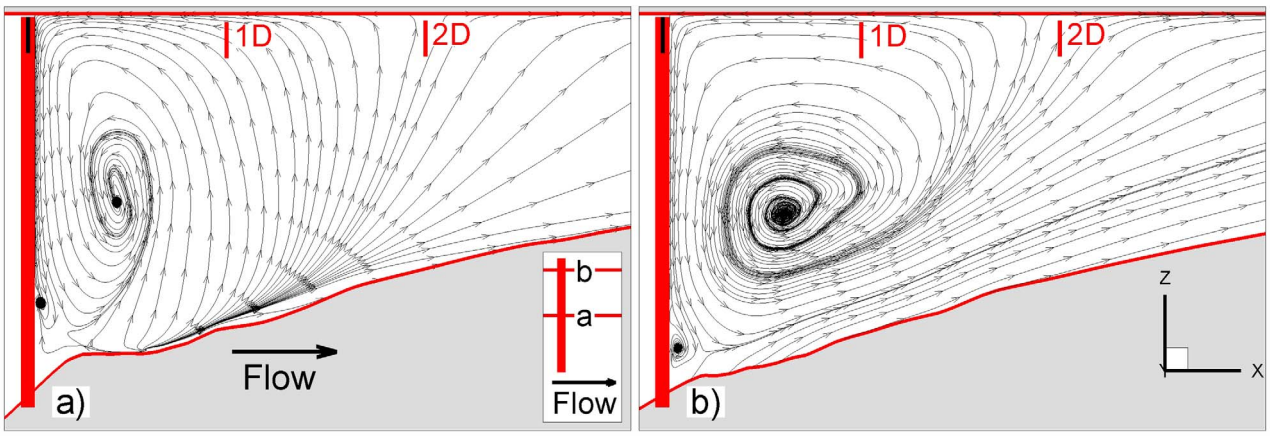

Figure 11. Visualization of the mean flow behind the cylinder using 2-D streamline patterns. (a) Symmetry (y/D = 0.0) plane; (b) y/D = 0.4D.

amplification of $\overline{u'v'}$ in Figure 10d is much smaller than that of $\overline{v'w'}$, highlighting the important role of the vertical velocity fluctuations. Interestingly, the mushroom shape of the region of high tke in Figure 9d is also present in the distribution of $\overline{u'w'}$ in Figure 10d, at about the same location. At all the four sections, the correlation between regions of high values of $\overline{u'w'}$ and $\overline{p'^2}$ is significantly smaller compared to that between regions of high values of $\overline{u'w'}$ and tke.

6. Vortical Content and Dynamics of the Detached Shear Layers and Near Wake

[45] Besides the sheets of vorticity on the two sides of the cylinder associated with the DSLs, the Q isosurface in Figure 8 shows the presence in the mean flow of two streamwise-oriented elongated eddies behind the cylinder. The two strong counter-rotating vortices are also visible in the 3-D streamline patterns shown in Figure 3. The 3-D streamline patterns in Figure 3b show the two eddies connect some distance (x ~ 0.6D) behind the cylinder. Compared to case CS where these vortices appear to originate at the back of the circular cylinder, in case RS the axes of the two eddies change orientation as they approach the cylinder and connect in the symmetry plane (see also Figure 11a that visualizes the mean flow in the symmetry plane behind the cylinder). In fact, it is probably more correct to talk about a U-shaped vortex rather than two separate counter-rotating vortices.

[46] Most of the flow particles from the incoming flow that are drawn inside one of the two streamwise oriented legs of the U-shaped vortex originate in the upper part of the channel, in a region centered around the symmetry plane. As they approach the upstream face of the cylinder (Figure 3a), the flow particles are deflected downward toward one of the sides of the cylinder (same as the one on which they approached the cylinder) and pass the cylinder very close to the bed (Figures 3b–3c). From there, they follow a trajectory parallel to the DSLs. One should point out the DSLs in the near bed region are oriented at an angle of approximately 60° with the downstream face of the cylinder and point toward the symmetry plane (see vorticity distribution at $\Delta z_d/D$ = 0.07 in Figure 13c). As they approach the symmetry plane, the flow particles are entrained upward into the segment of the U-shaped vortex core that is parallel to the downstream face of the cylinder. This segment of the U-shaped vortex is visualized in Figure 11 that shows 2-D streamline patterns in the symmetry (y/D = 0.0) and in the y/D = 0.3 planes. Once the particles are entrained into the core of the vortex on one of the two sides of the cylinder, they are advected into the streamwise-oriented legs and from there they are swept downstream. As the fluid particles follow a helicoidal trajectory inside the core of one of these two streamwise oriented legs, they also move closer to the free surface (Figure 3d).

[47] The advection of strong vortical eddies inside the DSLs and close to the bed (see Figure 13c) creates the conditions for the entrainment of sediment particles from behind the cylinder. If that happens, the presence of a relatively strong U-shaped vortex behind the cylinder ensures these particles will be convected away from the bed and then travel downstream for large distances with the fluid convected inside the legs of the vortex. Thus, the U-shaped vortex can play an important role for sediment transport by convecting sediment particles entrained from the sides of the cylinder and from behind it away from the scour hole. This is one of the main mechanisms that explain the growth of the scour hole behind the cylinder after the initial stages of the scour process.

[48] Figure 11b shows that in the mean flow the fluid particles situated close to the bed tend to move away from the bed in the region situated behind the cylinder. This helps the advection out of the scour hole of sediment particles entrained at the bed by the sweeping motions induced by the turbulent eddies passing at a small distance from the bed (e.g., see discussion of Figure 6). It also creates the conditions needed for the growth of the downstream part of the scour hole in the later stages of the scour process. It is also interesting to consider the differences between the 2-D streamline patterns in the symmetry plane in cases RS and CS. While in case CS [*Kirkil et al.*, 2009, Figure 10b] only the near-bed particles situated very close to the circular cylinder can be lifted by the mean upwelling motion toward the free surface, in case RF it is expected that most of the sediment particles entrained from the bed over a distance of

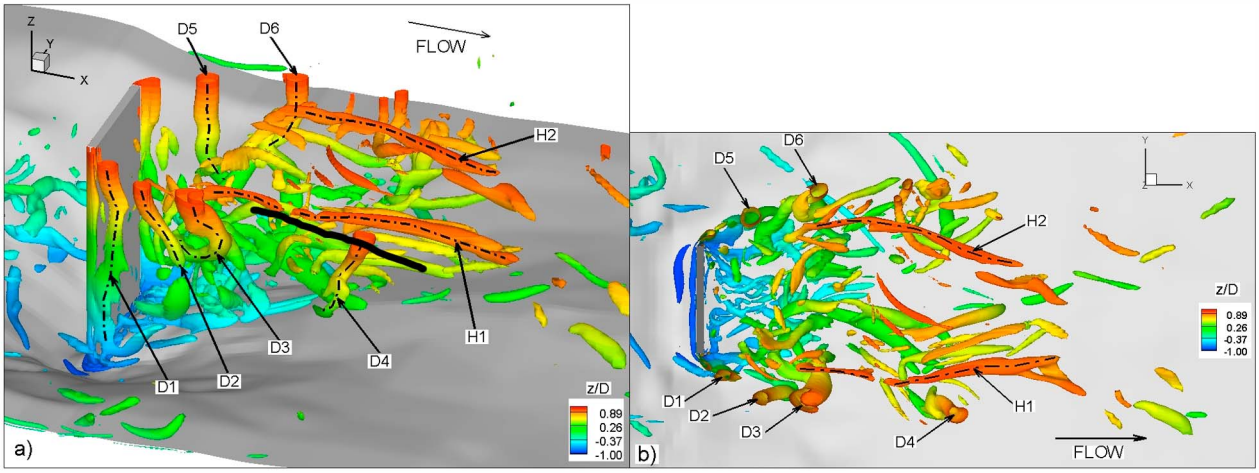

Figure 12. Visualization of the instantaneous vortical structure of the flow behind the cylinder using a Q isosurface. (a) Lateral view; (b) top view. The arrows point toward the axes of the vortex tubes shed in the DSLs (D) and the axes of the predominantly horizontal eddies (H) present in the near wake. The contours show the elevation with respect to the undeformed flat bed (z/D = 0.0).

approximately 2-D from the back of the rectangular cylinder will be entrained toward the free surface and from there into the core of the U-shaped vortex. The difference is obviously due to the presence in case RF of a strong vortex whose core is spanwise oriented and relatively parallel to the bed. This is also consistent with the smaller slope of the scour hole between the cylinder (x/D = 0) and x/D ~ 2D in case RF compared to case CS.

[49] Figure 12 visualizes the vortical structure of the instantaneous flow past the cylinder using a Q isosurface. Eddies in the form of vortex tubes (denoted D) form and are convected inside the DSLs. While the cores of these tubes are fairly vertical close to the free surface, they are strongly deformed as they approach the scoured bed. The lower parts of the tubes move predominantly toward the symmetry plane, consistent with the inward curving of the DSLs in the near bed region (Figure 13).

[50] A small junction vortex is present at the base of the upstream face of the cylinder (Figure 12b). The extremities of the junction vortex on the two sides of the cylinder interact with the eddies shed inside the DSLs in the near-bed region. This provides an additional mechanism that randomly disturbs the cores of the vortex tubes in the near-bed region.

[51] At larger distances behind the cylinder several elongated eddies (denoted H) are present, especially in the upper parts of the near-wake flow. Such eddies where also observed during the initial stages of the scour process in case RF [see *Kirkil and Constantinescu*, 2009, Figure 15]. While in the flat bed case most of these fairly horizontal eddies would cross the symmetry plane, in the deformed bed case these eddies are located only on one side of the cylinder. This suggests that behind the cylinder the eddies on the two sides of the symmetry plane interacts less. As will be seen from the following discussion, this is mainly due to the strong upwelling motions that develop once the scour hole is large enough to modify the way the DSLs on the two sides of the cylinder interact compared to the flat bed case.

[52] The vorticity magnitude contours in Figure 13 give more information on the change in the shape of the DSLs with the distance from the free surface and on the turbulence structure at different levels within the flow. The DSLs are oriented slightly outward near the free surface in Figure 13a. At middle-depth levels (z/D ~ 0.4), the DSLs become close to parallel to the streamwise direction. This orientation is the one expected for the flow past an infinitively long cylinder of rectangular shape. Inside the scour hole (Figures 13b–13c), the DSLs start curving inward toward the symmetry plane. This behavior is qualitatively similar to the one observed in case CS.

[53] In the mean flow, the angle between the cylinder and the DSLs is close to 60° very close to the scoured bed (Figure 13c). In the instantaneous flow, due the jittering of the eddies shed in the upstream part of the DSLs by the near-bed eddies and especially by the junction vortex, the angle is not constant. For example, in the snapshot showing the vorticity magnitude contours in the instantaneous flow in Figure 13c, the angle is close to 45°. The passage of highly energetic DSL eddies over the bed is one of the main mechanisms responsible for entrainment of sediment particles from the region situated immediately behind the cylinder. Once the DSL eddies approach the symmetry plane, they move relatively parallel to the symmetry plane against the mild slope of the scour hole. This induces the two elongated patches of vorticity on the two sides of the symmetry plane for $1 < x/D < 3$ in the mean flow (Figure 13c, mean flow). Inspection of the trajectories followed by the DSL eddies in the instantaneous flow shows that, despite interacting with each other from time to time, most of the eddies convected near the symmetry plane remain on the side on which they originated.

[54] Though the strong curving of the DSLs near the bed was also observed in case CS [see *Kirkil et al.*, 2009, Figure 11a], no streamwise oriented patches of high-vorticity magnitude were observed to form close to the symmetry plane. The eddies shed inside the DSLs maintain their coherence for much larger distances in the near-bed region in case RF. This is again consistent with the fact that the scour depth behind the cylinder and close to the symmetry plane decays at a milder rate with the distance from the

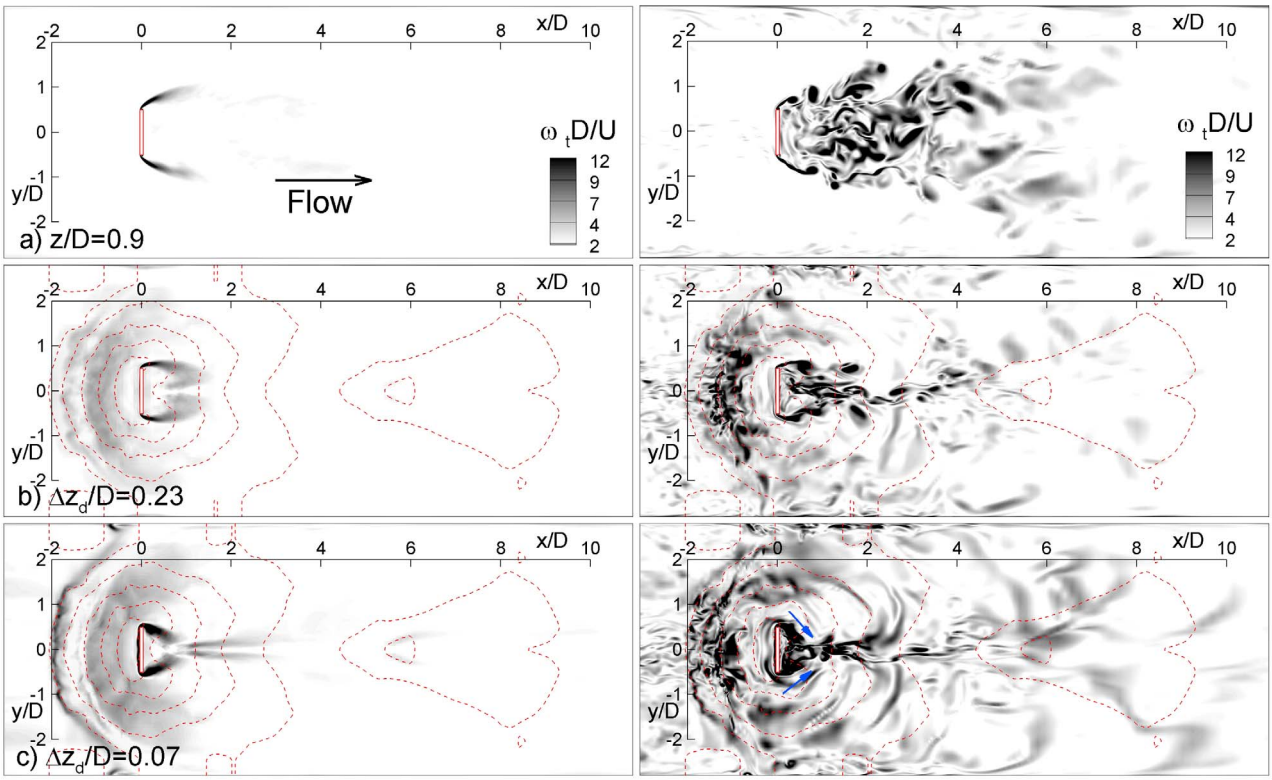

Figure 13. Vorticity magnitude ($\omega_t D/U$) contours in the (left) mean flow and (right) instantaneous flow. (a) Here z/D = 0.9; (b) $\Delta z_d/D = 0.23$; (c) $\Delta z_d/D = 0.07$. The arrows in Figure 13c show the direction at which the eddies are shed inside the DSLs close to the bed.

cylinder in the case of a rectangular cylinder. The reason for the stronger coherence of the DSLs in the near-bed region in case RS is the same as for the flat bed case (case RF). In both cases, the position of the flow separation on the cylinder is fixed (lateral edge) over the whole depth of the flow. This is, of course, not the case for a cylinder with a smooth shape in which the flow past the cylinder remains subcritical in the near-bed region even at high Reynolds numbers.

[55] The weak interaction between the DSLs on the two sides of the cylinder is even more evident at larger distances from the bed. In case RF, representative of the initial stages of the scour process, rollers formed and were shed in a quasi-regular way from each side of the cylinder as a result of the DSL on one side curving inward toward the symmetry plane and modifying the trajectory of the eddies shed in the DSL on the other side. These eddies would accumulate on one side of the back of the cylinder and form a new roller [see *Kirkil and Constantinescu*, 2009, Figure 13].

[56] As visualized in Figure 3, the presence of the scour hole in case RS induces the formation of the U-shaped vortex. The two streamwise-oriented legs convect fluid situated close to the symmetry plane and the bed toward the free surface. The strong upwelling motion of the flow close to the symmetry plane coupled with the presence and sense of rotation of the two legs of the U-shaped vortex forces the mean flow to be oriented away from the symmetry plane and pushes the two DSLs away from the symmetry plane. This explains the observed shape of the DSLs close to the free surface (Figure 13a) and the fact that most of the DSL eddies follow a trajectory that gets away from the symmetry plane. The interaction with the eddies convected away from the symmetry plane is the main mechanism responsible for the jittering of the DSL eddies away from the formation region and the bed, and for the amplification of the strength of the DSL eddies (e.g., due to merging phenomena). Strongly coherent DSL eddies are sometimes observed at large distances (x/D > 2) behind the cylinder (e.g., see Figure 14).

[57] Ultimately, the modifications of the dynamics of the eddies shed inside the DSLs due to the presence of the scour hole and of a relatively shallow channel are responsible for the different characteristics of the near-wake flow in case RS compared to case RF. The quasi-regular shedding of large-scale wake rollers observed in case RF is absent in case RS. As a result, the undular shape of the near-wake region in case RF is replaced by a shape that is

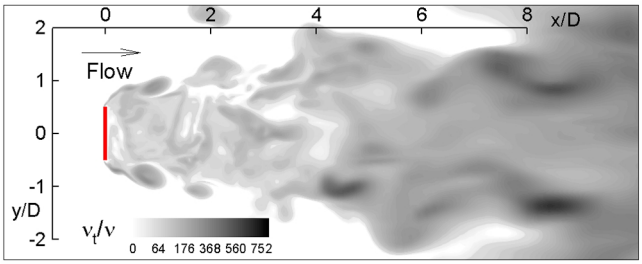

Figure 14. Visualization of the wake structure using eddy viscosity contours in a plane situated close to the free surface (z/D = 0.9).

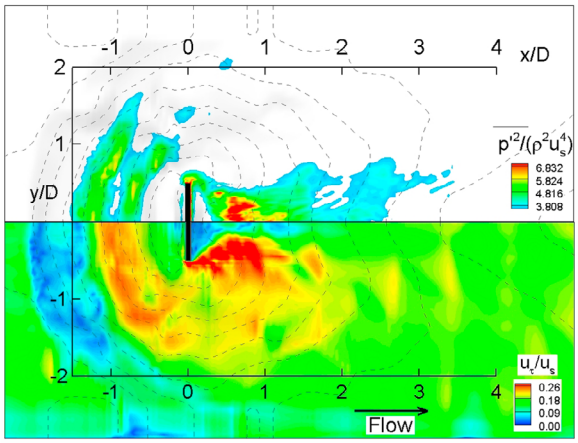

Figure 15. Distributions of the (top) pressure rms fluctuations, $\overline{p'^2}/(\rho^2 u_s^4)$, and (bottom) mean flow bed-friction velocity, u_τ/u_s, at the bed. The bathymetry isocontours are shown with dashed lines.

relatively symmetric with respect to the y/D = 0.0 plane. This can be observed from the comparison of *Kirkil and Constantinescu* [2009, Figure 14] and the eddy viscosity contours in Figure 14. Still, large-scale eddies are present in the near-wake region in case RS. As already discussed, most of these eddies originate in the DSLs. Thus, as opposed to case RF where the shedding of roller vortices in the wake was an important mechanism for sediment erosion downstream of the cylinder, the von Karman vortex shedding is not present in case RS. However, the large eddies shed relatively symmetrically in the two shear layers (see Figure 14 and discussion of Figure 16) can induce a noticeable amplification of the bed-friction velocity before they diffuse as they are advected away from the cylinder. Still, their coherence and capacity to entrain sediment is much smaller than that of the von Karman rollers observed in case RF. In a deeper flow, with a ratio between the channel depth and the maximum depth of the scour hole much larger than one, one expects the von Karman vortex shedding to be observed at least in the upper part of the water column. Whether in these cases the rollers will maintain their strong coherence in the deeper part of the water column is not clear. This shows that the importance of the large-scale vortex shedding as a mechanism for sediment erosion is highly dependent on the flow conditions, main geometrical parameters and the bathymetry. One should also mention the other extreme case which is encountered in marine environments subject to strong waves that induce an oscillatory flow around the cylinder. In this case scour is generally driven by the large-scale vortex shedding rather than the horseshoe vortex system. The change in the orientation of the DSL as the bed is approached and the fact that the shape of the near wake is not undular are two important common characteristics of the flow past cylinders with a large deformed bed that are independent of the shape of the cylinder.

7. Distributions of the Friction Velocity and Pressure RMS Fluctuations at the Bed

[58] As shown in Figure 15, the largest values of $\overline{p'^2}$ at the bed are observed behind the cylinder, at x/D ~ 0.65. Toward the cylinder, high $\overline{p'^2}$ values are predicted in the region where the vortex tubes are convected inside the DSL, close to the scoured bed. In the downstream direction, the patch of high $\overline{p'^2}$ values extends up to x ~ 3-D. One should also notice the amplification of $\overline{p'^2}$ beneath the region where the core of HV1 is subject to bimodal oscillations. The peak values in this region are approximately 4.9 $\rho^2 u_s^4$ or $0.035\rho^2 U^4$.

[59] The distribution of $\overline{p'^2}$ in the region situated downstream of the cylinder is significantly different than the one observed in the flat bed case [see *Kirkil and Constantinescu*, 2009, Figure 16a] in which the region of large $\overline{p'^2}$ values started at the face of the cylinder and the peak values were observed inside the DSLs. More important, the nondimensional values in the region of high $\overline{p'^2}$ values are close to 1 order of magnitude lower in case RS compared to case RF. This is consistent with the fact that the bathymetry in case RS corresponds to conditions near equilibrium. Compared to case CS [see *Kirkil et al.*, 2009, Figure 14a], the nondimensional values of $\overline{p'^2}$ are comparable in the regions of high pressure fluctuations, but the position of these regions is different, as in case CS the largest values of $\overline{p'^2}$ were observed close to the face of the cylinder for $50° < |\varphi| < 160°$.

[60] The bed-friction velocity distribution in the mean flow (Figure 15b) shows that the largest values of u_τ are situated in the small acceleration region at the base of the two sides of the cylinder, and in the region where DSL eddies are shed at a small distance from the bed. Similar to $\overline{p'^2}$, relatively large values of u_τ are observed beneath the region where the core of HV1 undergoes bimodal oscillations. The values of u_τ remain relatively high downstream of the cylinder (x/D > 0) beneath the legs of HV1. In fact, this region of high u_τ merges with the one induced by the passage of eddies convected inside the DSLs.

[61] The distribution of u_τ in the instantaneous flow in Figure 16 shows that values comparable to the ones observed in the region where eddies are shed inside the DSLs can be present beneath part of the core of HV1, inside the upstream part of the scour hole, and even beneath the downstream part of the legs of HV1 that move predominantly against the local slope of the scour hole. At the time instance at which the distribution of u_τ is shown in Figure 16, two strong eddies originating from the legs of HV1 are moving against the local slope of the scour hole on both sides of the cylinder. Meanwhile, the coherence of HV1 is relatively high in front of the cylinder while that of its legs is small. Two patches of relatively high values of u_τ are present on both sides of the symmetry plane for $2.5 < x/D < 3.5$. In most cases, these patches form as a result of the interaction between a strong DSL eddy and a streak of vorticity detaching from the legs of HV1.

[62] Overall, there is a remarkable level of symmetry in the positions of the regions of high u_τ values with respect to the symmetry plane. This is the opposite of what was observed in the case RF in which the alternate shedding of the large-scale rollers from the two sides of the rectangular cylinder controlled the position of the regions of high u_τ values [see *Kirkil and Constantinescu*, 2009, Figure 17a]. This is true not only for the wake region, but also for the region situated upstream of the cylinder where the changes in the coherence of HV1 were controlled to a large degree by its interaction with the latest roller shed from the cylinder.

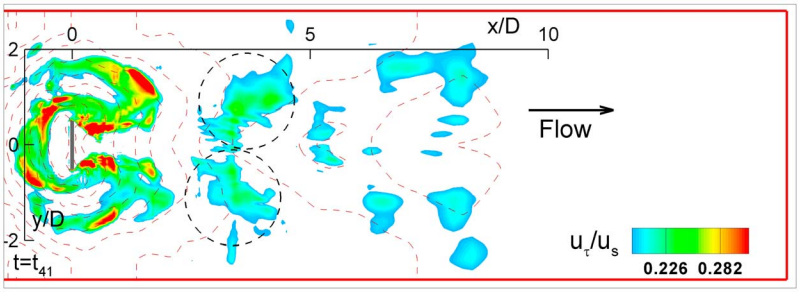

Figure 16. Distribution of the bed-friction velocity, u_τ/u_s, in the instantaneous flow. The two dashed circles show two patches of high u_τ/u_s disposed symmetrically with respect to the symmetry plane that are moving downstream with about the same streamwise velocity. The bathymetry isocontours are shown with dashed lines.

[63] The four frames in Figure 17 visualize the temporal evolution of u_τ as a result of the movement of the downstream leg of HV1 away from the cylinder, followed by the detachment of a streak of vorticity and its advection away from the cylinder. Interestingly, this phenomenon occurs simultaneously on both sides of the cylinder in Figure 17, though the strength of the patch of high u_τ values on the two sides is different. In Figure 17a, the coherence of HV1 is large around the two sides of the cylinder, but is small in front of the cylinder. After 0.5D/U (Figure 17b), the two sides of HV1 (see arrows) have separated and are moving away from the cylinder and against the slope of the scour hole. After another 0.4D/U (Figure 17c), the coherence of HV1 in front of the cylinder increases again, but the core of HV1 is situated in the deeper part of the scour hole and its legs are situated very close to the sides of the cylinder. Meanwhile, the downstream movement of the two patches of high u_τ values induced by the advection of eddies that detached from HV1 continues. Finally, in Figure 17d a compact region of high u_τ values is observed beneath the core of HV1, including beneath its legs that are getting very close to the DSLs before starting moving away from them.

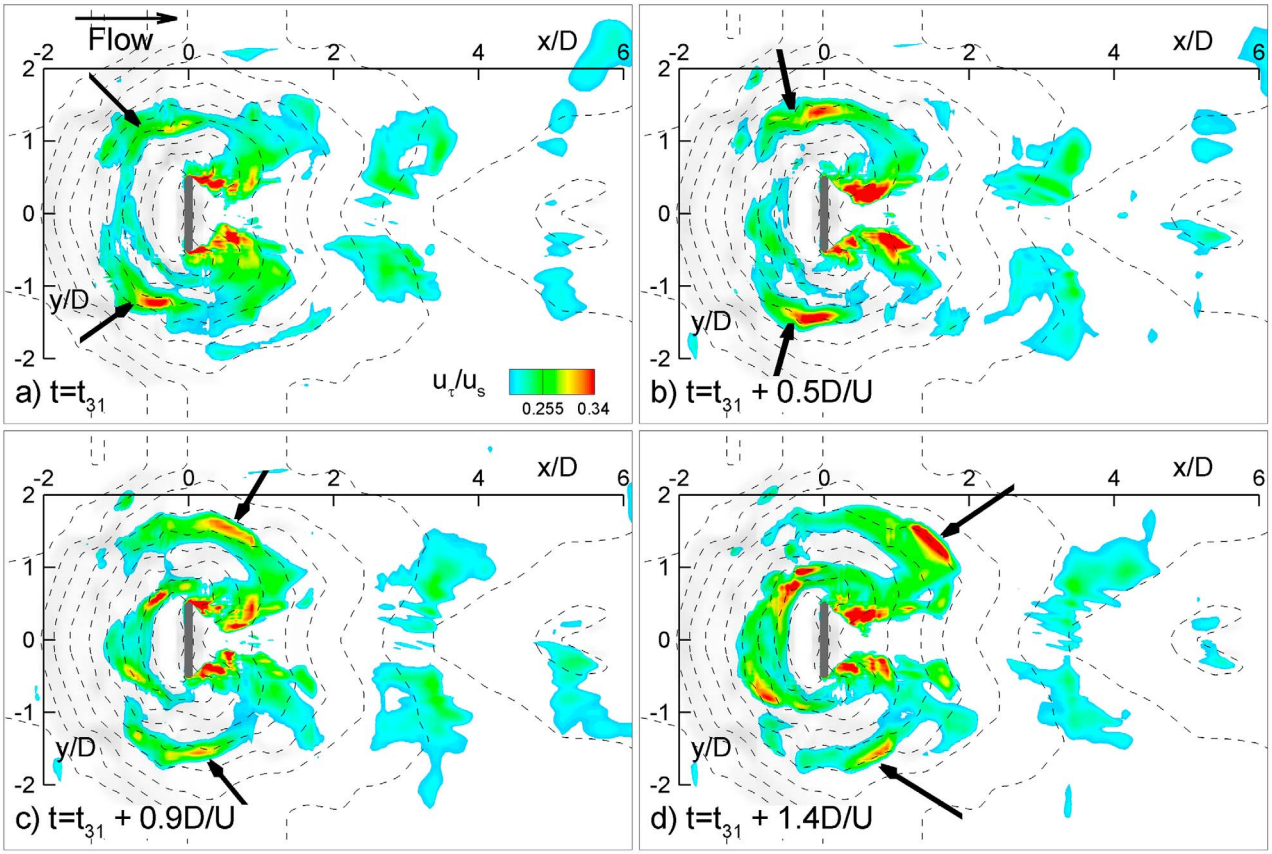

Figure 17. Temporal evolution of the bed-friction velocity, u_τ/u_s, inside the scour hole. (a) Here $t = t_{31}$; (b) $t = t_{31} + 0.5D/U$; (c) $t = t_{31} + 0.9D/U$; (d) $t = t_{31} + 1.4D/U$. The arrows point toward the legs of the main necklace vortex that interact fairly symmetrically with the eddies forming in the DSLs. The bathymetry isocontours are shown with dashed lines.

[64] The sequence described above is representative of the dominant way in which the interactions between the legs of HV1 and the DSLs take place in case RS. The fact that these interactions occur fairly regularly is a similarity with case RF and a difference with case CS, in which these interactions occurred in a much less organized way and the level of amplification of u_τ beneath the wake eddies decayed sharply with the distance from the circular cylinder. Still, there are some important differences between cases RS and RF. At conditions corresponding to the start of the scour process (case RF), the interactions between the legs of HV1 and the DSL were antisymmetrical, in the sense that only the leg on one side of the rectangular cylinder interacted with the DSL on the side where a new roller was forming. The level of amplification of u_τ beneath the large eddies shed in the wake on both sides of the cylinder is smaller in case RS compared to case RF. This is expected, as in case RS the scour is very close to equilibrium. Meanwhile, that is not expected to be the case after the initial stages of the scour process, when the scour hole is relatively large, but still far from equilibrium.

[65] The lateral movements of the legs of HV1 away from the sides of the rectangular cylinder and from the DSLs are mainly responsible for the observed amplification of u_τ in the mean flow on the lateral sides of the scour hole. The instantaneous values of u_τ at a specific location in this region can be as high as those observed beneath the DSL eddies. However, as the instantaneous u_τ values correlate with the presence, or not, of a strong vertical eddy above a specific location and the frequency at which these eddies are passing is relatively low (of the order of 1–4 D/U), the values of u_τ in the mean flow (Figure 15) are significantly lower than those observed at locations at which DSL eddies are convected with a relatively high frequency (Figure 16).

8. Summary and Concluding Remarks

[66] The instantaneous and mean flow fields obtained from a DES simulation at a channel Reynolds number of 240,000 were used to investigate the dynamics of the coherent structures in the flow past a high aspect ratio rectangular cylinder with scoured bed corresponding to conditions toward the end of the scour process. The problem has direct applications for the study of erosion and deposition phenomena at bridge piers of similar shape.

[67] The present work highlights the need to understand and differentiate the mechanisms causing scour around bluff body obstacles of different shapes and at different stages of the scour process. Comparison of the simulations of flow past rectangular cylinders with flat bed and with a large scour hole allowed to better understand the changes in the mechanisms driving the scour around the in-stream obstruction between the initial and later stages of the scour process, when the scour hole is large enough to stabilize the large-scale oscillations HV system and to modify the dynamics of large-scale eddies shed in the near wake. Comparison of the simulations with rectangular and circular cylinders with a large scour hole allowed us to understand the changes in the wake flow during the later stages of the scour process between cases in which the separation line of the attached boundary layer on the cylinder is dictated by the flow and its position can vary with the distance from the bed (circular cylinders), and cases in which the separation line is fixed (e.g., edge of the rectangular cylinder) and dictated by the geometry of the cylinder.

[68] Similar to the flat bed case and to the case of the flow past a circular cylinder with scour hole, the main necklace vortex of the HV system was observed to undergo large-scale bimodal oscillations in the region situated in front of the cylinder and close to its sides. This shows that bimodal oscillations of the necklace vortices are present at all stages of the scour and deposition process and, thus, are a general characteristic of flow past in-stream obstacles, even if the bed is mobile. The transition mechanism between the two modes presents some differences with the classical one proposed by *Devenport and Simpson* [1990] for bluff bodies mounted on flat surfaces. The differences are due to the presence of a highly scoured bed in between the line where the incoming boundary layer separates and the upstream face of the cylinder. The change from one mode to the other was related to the ejection away from the bed of a tongue of vorticity of opposite sign to the vorticity inside the necklace vortex. The ejection occurred due to the interaction of the tongue of vorticity with the eddies convected from the separated incoming boundary layer and with the eddies convected with the jet-like flow away from the cylinder. Simulation results showed the transition to the back-flow mode can also be triggered by the advection of high-momentum and high-vorticity eddies first with the down-flow toward the toe of the cylinder and then away from the cylinder, as part of the jet-like flow. This is different from the mechanism that is generally observed at in-stream obstacles mounted on a flat bed where the transition to the back-flow mode is triggered by injection of high-momentum low-vorticity eddies from the regions situated away from the bed.

[69] In the case of a rectangular cylinder, the distributions of the tke in the sections where the coherence of the main necklace vortex was high were qualitatively similar to the ones observed in the case of a circular cylinder with deformed bed and to the one measured by *Devenport and Simpson* [1990] in front of a wing-shaped body at a comparable Reynolds number. Meanwhile, the distributions of the pressure rms fluctuations showed that besides the bimodal region, large $\overline{p'^2}$ values were present inside the upstream part of the jet-like flow region, especially in sections situated closer to the sides of the cylinder. A noticeable decay of the turbulence intensity in the HV region was observed only after the necklace vortex was swept past the sides of the cylinder.

[70] Compared to the case of a circular cylinder where the intensity of the HV system decayed monotonically with the distance from the upstream symmetry plane, in the case of a high aspect ratio rectangular cylinder, the turbulence intensity inside the HV region varied little between the symmetry plane and planes cutting through the sides of the cylinder. This is somewhat expected, as the flow past a high aspect ratio rectangular cylinder starts resembling the flow past a vertical groyne (or bridge abutment) away from the lateral wall on which the groyne is mounted. *Koken and Constantinescu* [2008a, 2008b] have shown that the coherence of the HV system peaks around sections situated close to the extremity of the groyne.

[71] Different degrees of turbulence amplification and qualitative differences in the turbulence distribution within the upstream part of the scour hole were observed between rectangular and circular cylinders not only during the later stages of the scour process but also during the initial stages of the scour process [*Kirkil and Constantinescu*, 2009]. The differences during the final stages of the scour process allowed understanding why the scour hole was larger and deeper (e.g., by about 15% for the nondimensional scour depth) for the cylinder with a higher degree of bluntness. The turbulence amplification was comparable in vertical sections situated in between the symmetry plane and the edge of the rectangular cylinder. This is a main reason why the depth of the scour hole, close to the upstream face of the rectangular cylinder, did vary little in the spanwise direction. However, one anticipates that as the ratio between the width of the rectangular cylinder and the water depth is further increased (e.g., transition to the wide pier regime), the largest turbulence amplification and thus the intensity of the bimodal oscillations will peak at sections situated close to the two extremities of the rectangular cylinder. In this case, the largest scour will occur around the edges of the cylinder rather than close to the symmetry plane. This is a direct example of how the changes in the turbulent structure can explain the observed scour patterns at cylinders of various shapes.

[72] The interaction of the legs of the necklace vortices with the eddies convected away from the cylinder in the near-bed region and with the DSL eddies resulted in the formation of streaks of concentrated vorticity. At most time instances these streaks were oriented parallel to the lines of constant bed elevation and moved against the local slope of the bed, at a small distance from it. In some cases an array of streaks formed on one or on both sides of the cylinder. This means the advection of the streaks can play an important role in the entrainment of sediment from the scoured bed and is one of the main mechanisms responsible for the lateral and downstream growth of the scour hole in the later stages of the scour process.

[73] The main coherent structures behind the cylinder were the two streamwise oriented legs of a U-shaped vortex. Such eddies were also observed in the case of the flow past a circular cylinder with scoured bed. In the latter case they attached to the back of the cylinder, rather than merge together, and their coherence was lower. The main role of these streamwise counter-rotating eddies is to induce a strong upward motion of the flow in the region close to the symmetry plane and to significantly reduce the interaction between the DSLs on the two sides of the cylinder. As the eddies convected by the legs of the U-shaped vortex approach the free surface, they are convected away from the symmetry plane and push the DSLs outward. This is the main reason why the alternate (antisymmetrical) shedding of large-scale rollers from the two sides of the cylinder observed in the flat bed case was suppressed. The undular shape of the near wake region present in the flat bed case was replaced by a shape that is relatively symmetric with respect to the symmetry plane.

[74] Similar to the case of the flow past a circular cylinder with deformed bed, the DSLs curved strongly toward the back of the cylinder as the bed is approached. The angle at which the energetic DSL eddies are convected away from the sides of the cylinder is variable in time. This provides another mechanism that explains the growth of the scour hole behind the cylinder.

[75] The pressure rms fluctuations in the region of high $\overline{p'^2}$ values situated behind the cylinder were close to 1 order of magnitude lower in the deformed bed case compared to the flat bed case, which is consistent with the fact that the bathymetry in the deformed bed case corresponds to conditions near equilibrium. The largest values of the bed-friction velocity in the mean flow occurred in the small acceleration region at the base of the two sides of the cylinder, and in the region where DSL eddies are shed at a small distance from the bed.

[76] In the instantaneous flow, patches of relatively large bed-friction velocity were observed on both sides of the cylinder. These patches were induced by the relatively regular interactions of the large quasi-two-dimensional eddies forming in the downstream part of the two DSLs with the legs of the main necklace vortex. These interactions occurred relatively symmetrically on both sides of the cylinder. This is the opposite of what was observed in the flat bed case in which the alternate shedding of the large-scale rollers from the two sides of the cylinder controlled the position of the regions of high u_τ values in the near wake.

[77] The fact that in the case of a rectangular cylinder the large-scale quasi-2-D eddies shed in the wake maintained their coherence up to the bed surface during the whole duration of the scour process, despite significant changes in the wake structure, is a direct consequence of the flow separating on the cylinder at a fixed location over the whole depth. This greatly increases the capacity of these eddies to entrain sediment and explains the larger size of the scour hole behind the cylinder and the larger speed at which the scour process takes place in the experiment conducted with a rectangular cylinder compared to the one in which the cylinder was circular. Meanwhile, the fact that in the experiments the maximum scour depth in front of the cylinder, when expressed nondimensionally with the projected width of the cylinder as the length scale, was deeper for a rectangular cylinder is mainly due to the larger degree of bluntness of the rectangular cylinder which creates the conditions for the formation of a more coherent and stable main necklace vortex. Experimental observations and comparison of the simulations with flat and deformed bed showed that the differences in the circulation and coherence of the main necklace vortex between rectangular and circular cylinders are the largest during the initial stages of the scour process (this also explains the rapid rate of the growth of scour hole during the initial stages of the scour process at rectangular cylinders) and decay gradually with the development of the scour hole. This is mainly because the effect of the degree of bluntness of the in-stream obstacle on the interaction between the downflow and the bed region situated close to the upstream face of the obstacle is the largest when the bed is flat.

[78] This study highlights the need for a detailed understanding of the dynamics of the large-scale coherent structures induced by the presence of in-stream obstacles in a turbulent surrounding flow, as a prerequisite to understand local scour phenomena. The present study shows that the changes in the scour depth as a result of a change in the shape of the cylinder are due to both quantitative changes

in the coherence of the main coherent structures driving the scour but also to qualitative differences in the mechanisms that drive the scour process on the sides and behind the cylinder and the mechanisms responsible for the transport of the sediment entrained in front of the cylinder away from the scour hole region. As such, it highlights the purely empirical nature of the approach based on deriving obstruction shape factor coefficients that will correct the scour depth predicted for the case of a circular cylinder (e.g., it is not clear how these shape coefficients should vary with the degree of bluntness of the obstacle and whether a general bluntness parameter for a cylinder of arbitrary shape can be defined) and the need for incorporating in scour prediction methods, at the minimum, some information on the structure and coherence of the necklace vortex system after the scour hole has formed.

[79] In a larger context, this study adds to recent work performed to understand the interactions between macro-turbulent flow structures and large-scale flow obstructions (e.g., large bed roughness elements in the form of pebble clusters, see *Lacey and Roy* [2007]) present at the bed of erodible channels. Our long-term goal is to use of DES rather than RANS [see, e.g., *Zeng et al.*, 2008, 2010] to predict flow, sediment transport and bathymetry evolution in open channels with or without large-scale obstructions.

[80] **Acknowledgments.** The authors would like to thank Robert Ettema for his advice on various aspects of this research and the National Center for High Performance Computing (NCHC) in Taiwan, in particular W.F. Tsai for providing the computational resources needed to perform some of the simulations as part of the collaboration program between NCHC and IIHR-Hydroscience and Engineering. The first author would also like to acknowledge the Lawrence Livermore National Laboratory. Lawrence Livermore National Laboratory is managed by Lawrence Livermore National Security, LLC for the U.S. Department of Energy under contract DE-AC52-07NA27344.

References

Ahmed, F., and N. Rajaratnam (1998), Flow around bridge piers, *J. Hydraul. Eng.*, *124*(3), 288–300, doi:10.1061/(ASCE)0733-9429(1998)124:3(288).

Chang, K., G. Constantinescu, and S. O. Park (2007), Assessment of predictive capabilities of detached eddy simulation to simulate flow and mass transport past open cavities, *J. Fluids Eng.*, *129*(11), 1372–1383, doi:10.1115/1.2786529.

Choi, S. U., and W. Yang (2002), Numerical simulation of 3-D flows around bridge piers, paper presented at First International Conference on Scour of Foundations, pp. 206–213, Texas A&M Univ., College Station, Tex.

Constantinescu, G. S., and K. D. Squires (2003), LES and DES investigations of turbulent flow over a sphere at Re = 10,000, *Flow Turbul. Combus.*, *70*, 267–298, doi:10.1023/B:APPL.0000004937.34078.71.

Constantinescu, G. S., and K. D. Squires (2004), Numerical investigation of the flow over a sphere in the subcritical and supercritical regimes, *Phys. Fluids*, *16*(5), 1449–1467, doi:10.1063/1.1688325.

Constantinescu, G., M. C. Chapelet, and K. D. Squires (2003), Turbulence modeling applied to flow over a sphere, *AIAA J.*, *41*(9), 1733–1742, doi:10.2514/2.7291.

Dargahi, B. (1990), Controlling mechanism of local scouring, *J. Hydraul. Eng.*, *116*(10), 1197–1214, doi:10.1061/(ASCE)0733-9429(1990)116:10(1197).

Devenport, W. J., and R. L. Simpson (1990), Time-dependent and time-averaged turbulence structure near the nose of a wing-body junction, *J. Fluid Mech.*, *210*, 23–55, doi:10.1017/S0022112090001215.

Dey, S., and R. V. Raikar (2007), Characteristics of horseshoe vortex in developing scour holes at piers, *J. Hydraul. Eng.*, *133*(4), 399–413, doi:10.1061/(ASCE)0733-9429(2007)133:4(399).

Dey, S., S. K. Bose, and G. Sastry (1995), Clearwater scour at circular piers: A model, *J. Hydraul. Eng.*, *121*(12), 869–876, doi:10.1061/(ASCE)0733-9429(1995)121:12(869).

Dubief, Y., and F. Delcayre (2000), On coherent vortex identification in turbulence, *J. Turbul.*, *1*, 11.

Ettema, R., B. W. Melville, and B. Barkdoll (1998), Scale effects in pier-scour experiments, *J. Hydraul. Eng.*, *124*(6), 639–642, doi:10.1061/(ASCE)0733-9429(1998)124:6(639).

Ettema, R., G. Kirkil, and M. Muste (2006), Similitude of large-scale turbulence in experiments on local scour at cylinders, *J. Hydraul. Eng.*, *132*(1), 33–40, doi:10.1061/(ASCE)0733-9429(2006)132:1(33).

Fael, C. M. S., G. Simarro-Grande, J. P. Martin-Vide, and A. H. Cardoso (2006), Local scour at vertical-wall abutments under clear water flow conditions, *Water Resour. Res.*, *42*, W10408, doi:10.1029/2005WR004443.

Graf, W. H., and I. Istiarto (2002), Flow pattern in the scour hole around a cylinder, *J. Hydraul. Res.*, *40*(1), 13–20, doi:10.1080/00221680209499869.

Hardy, R. J., S. N. Lane, R. I. Ferguson, and D. R. Parsons (2007), Emergence of coherent flow structures over a gravel surface: A numerical experiment, *Water Resour. Res.*, *43*, W03422, doi:10.1029/2006WR004936.

Hinsch, K. D. (2002), Holographic particle image velocimetry, *Meas. Sci. Technol.*, *13*, R61–R72, doi:10.1088/0957-0233/13/7/201.

Keylock, C. J., R. J. Hardy, D. R. Parsons, R. I. Ferguson, S. N. Lane, and K. S. Richards (2005), The theoretical foundations and potential for large eddy simulation in fluvial geomorphic and sedimentological research, *Earth Sci. Rev.*, *71*, 271–304, doi:10.1016/j.earscirev.2005.03.001.

Kirkil, G., and G. Constantinescu (2009), Nature of flow and turbulence structure around an in-stream vertical plate in a shallow channel and the implications for sediment erosion, *Water Resour. Res.*, *45*, W06412, doi:10.1029/2008WR007363.

Kirkil, G., S. G. Constantinescu, and R. Ettema (2008), Coherent structures in the flow field around a circular cylinder with scour hole, *J. Hydraul. Eng.*, *134*(5), 572–587, doi:10.1061/(ASCE)0733-9429(2008)134:5(572).

Kirkil, G., G. Constantinescu, and R. Ettema (2009), DES investigation of turbulence and sediment transport at a circular pier with scour hole, *J. Hydraul. Eng.*, *135*(11), 888–901, doi:10.1061/(ASCE)HY.1943-7900.0000101.

Koken, M., and G. Constantinescu (2008a), An investigation of the flow and scour mechanisms around isolated spur dikes in a shallow open channel: 1. Conditions corresponding to the initiation of the erosion and deposition process, *Water Resour. Res.*, *44*, W08406, doi:10.1029/2007WR006489.

Koken, M., and G. Constantinescu (2008b), An investigation of the flow and scour mechanisms around isolated spur dikes in a shallow open channel: 2. Conditions corresponding to the final stages of the erosion and deposition process, *Water Resour. Res.*, *44*, W08407, doi:10.1029/2007WR006491.

Koken, M., and G. Constantinescu (2009), An investigation of the dynamics of coherent structures in a turbulent channel flow with a vertical sidewall obstruction, *Phys. Fluids*, *21*, 085104, doi:10.1063/1.3207859.

Krajnovic, S., and L. Davidson (2002), Large eddy simulation of the flow about a bluff body, *AIAA J.*, *40*, 927–936, doi:10.2514/2.1729.

Lacey, R. W. J., and A. G. Roy (2007), A comparative study of the turbulent flow field with and without a pebble cluster in a gravel river bed, *Water Resour. Res.*, *43*, W05502, doi:10.1029/2006WR005027.

Laursen, E. M., and A. Toch (1956), Scour around bridge piers and abutments, *Bull. 4*, Iowa Highw. Res. Board, Ames.

Melville, B. W., and S. E. Coleman (2000), *Bridge Scour*, Water Res. Publ., Littleton, Colo.

Raikar, R. V., and S. Dey (2008), Kinematics of horseshoe vortex development in an evolving scour hole at a square cylinder, *J. Hydraul. Res.*, *46*(2), 247–264, doi:10.1080/00221686.2008.9521859.

Rodi, W. (1997), Comparison of LES and RANS calculations of the flow around bluff bodies, *J. Wind Eng. Ind. Aerodyn.*, *69–71*, 55–75, doi:10.1016/S0167-6105(97)00147-5.

Roulund, A., B. M. Sumer, J. Fredsoe, and J. Michelsen (2005), Numerical and experimental investigation of flow and scour around a circular pile, *J. Fluid Mech.*, *534*, 351–401, doi:10.1017/S0022112005004507.

Roy, A. G., T. Buffin-Belanger, H. Lamarre, and A. D. Kirkbride (2004), Size, shape and dynamics of large-scale turbulent flow structures in a gravel-bed river, *J. Fluid Mech.*, *500*, 1–27, doi:10.1017/S0022112003006396.

Spalart, P. R. (2000a), Strategies for turbulence modeling and simulations, *Int. J. Heat Fluid Flow*, *21*, 252–263, doi:10.1016/S0142-727X(00)00007-2.

Spalart, P. R. (2000b), Trends in turbulence treatments, *AIAA Pap.*, 2000–2306.

Sumer, B. M., and J. Fredsoe (2002), *The Mechanics of Scour in the Marine Environment*, World Sci., River Edge, N. J.

Unger, J., and W. H. Hager (2006), Downflow and horseshoe vortex characteristics of sediment embedded bridge piers, *Exp. Fluids*, *42*, 1–19, doi:10.1007/s00348-006-0209-7.

Yeh, C. C. (1996), The three-dimensional flow fields around square and circular cylinders mounted vertically on a flat plate, Master thesis, Dep. of Civil Eng., Natl. Chung-Hsing Univ., Taiwan.

Yorozuya, A. (2005), Scour at bridge abutments with erodible embankments, Ph.D. thesis, Dep. of Civil and Environ. Eng., Univ. of Iowa, Iowa City.

Zeng, J., S. G. Constantinescu, and L. Weber (2008), A 3-D non-hydrostatic model to predict flow and sediment transport in loose-bed channel bends, *J. Hydraul. Res.*, *46*(3), 356–372, doi:10.3826/jhr.2008.3328.

Zeng, J., G. Constantinescu, and L. Weber (2010), 3-D calculations of equilibrium conditions in loose-bed open channels with significant suspended sediment load, *J. Hydraul. Eng.*, *136*(9), 557–571, doi:10.1061/(ASCE)HY.1943-7900.0000213.

G. Constantinescu, Stanley Hydraulics Laboratory, Civil and Environmental Engineering Department, IIHR-Hydroscience and Engineering, University of Iowa, Iowa City, IA 52242, USA. (sconstan@engineering.uiowa.edu)

G. Kirkil, Atmospheric, Earth and Energy Division, Lawrence Livermore National Laboratory, PO Box 808, L-103, Livermore, CA 94551, USA.